Bioactive Materials 46 (2025) 195–212

Contents lists available at ScienceDirect

Bioactive Materials

journal homepage: www.keaipublishing.com/en/journals/bioactive-materials

Copper doped bioactive glass promotes matrix vesicles-mediated biomineralization via osteoblast mitophagy and mitochondrial dynamics during bone regeneration

Ziji Ling [a,b,c], Xiao Ge [a,b,c], Chengyu Jin [a,b,c], Zesheng Song [a,b,c], Hang Zhang [a,b,c], Yu Fu [a,b,c], Kai Zheng [b,c], Rongyao Xu [a,b,c,**], Hongbing Jiang [a,b,c,*]

[a] Department of Oral and Maxillofacial Surgery, Affiliated Hospital of Stomatology, Nanjing Medical University, 210029, Nanjing, China
[b] State Key Laboratory Cultivation Base of Research, Prevention and Treatment for Oral Diseases, Nanjing Medical University, 210029, Nanjing, China
[c] Jiangsu Province Engineering Research Center of Stomatological Translational Medicine, Nanjing Medical University, 210029, Nanjing, China

ARTICLE INFO

Keywords:
Copper
Mesoporous bioactive glass
Mitophagy
Biomineralization
Bone regeneration

ABSTRACT

Bone defect repair remains a great challenge in the field of orthopedics. Human body essential trace element such as copper is essential for bone regeneration, but how to use it in bone defects and the underlying its mechanisms of promoting bone formation need to be further explored. In this study, by doping copper into mesoporous bioactive glass nanoparticles (Cu-MBGNs), we unveil a previously unidentified role of copper in facilitating osteoblast mitophagy and mitochondrial dynamics, which enhance amorphous calcium phosphate (ACP) release and subsequent biomineralization, ultimately accelerating the process of bone regeneration. Specifically, by constructing conditional knockout mice lacking the autophagy gene *Atg5* in osteogenic lineage cells, we first confirmed the role of Cu-MBGNs-promoted bone formation via mediating osteoblast autophagy pathway. Then, the *in vitro* studies revealed that Cu-MBGNs strengthened mitophagy by inducing ROS production and recruiting PINK1/Parkin, thereby facilitating the efficient release of ACP from mitochondria into matrix vesicles for biomineralization during bone regeneration. Moreover, we found that Cu-MBGNs promoted mitochondrion fission via activating dynamin related protein 1 (Drp1) to reinforce mitophagy pathway. Together, this study highlights the potential of Cu-MBGNs-mediated mitophagy and biomineralization for augmenting bone regeneration, offering a promising avenue for the development of advanced bioactive materials in orthopedic applications.

1. Introduction

Bone defect, a common manifestation caused by trauma, tumors or genetic malformations, severely impacts patients' appearance and quality of life [1–3]. Despite the bone's remarkable capacity for self-healing and restoration, achieving complete regeneration and mineralization of the defect site is a time-consuming process [4,5]. The strategy of accelerating mineralization to enhance bone defect repair has emerged as a promising approach that is widely studied in recent bone tissue engineering research [6]. The mineralization of bone involves a gradual process in which amorphous calcium phosphate (ACP) infiltrates collagen fibrils, undergoes phase transformation, and matures into bone mineral crystals [7]. This process orchestrated by osteoblasts encompasses a multitude of subcellular and extracellular activities, including intracellular mineral formation, release of ACP into the extracellular matrix (ECM), as well as intricate communication within organelles such as mitochondria and the endoplasmic reticulum [8–12]. Mitophagy, a critical process, serves not only as a component of mitochondria quality control but also acts as a pivotal step in ACP's intracellular transportation discovered in osteoblasts. The aggregation of ACP reduces mitochondrial membrane potential (MMP), triggering PINK1/Parkin-mediated mitophagy for excretion of ACP into the

Peer review under the responsibility of KeAi Communications Co., Ltd.
* Corresponding author. State Key Laboratory Cultivation Base of Research, Prevention and Treatment for Oral Diseases, Nanjing Medical University, 140 Hanzhong Road, 210029, Nanjing, China.
** Corresponding author. Department of Oral and Maxillofacial Surgery, Affiliated Hospital of Stomatology, Nanjing Medical University, 210029, Nanjing, China.
E-mail addresses: rongyaoxu@njmu.edu.cn (R. Xu), jhb@njmu.edu.cn (H. Jiang).

https://doi.org/10.1016/j.bioactmat.2024.12.010
Received 25 August 2024; Received in revised form 5 November 2024; Accepted 6 December 2024

extracellular matrix [10,13,14]. Recently, studies have focused on promoting autophagy or mitophagy to mitigate oxidative stress, maintain cellular homeostasis, and enhance osteogenic differentiation and bone regeneration [15–17]. However, few studies have utilized mitophagy mediated biomineralization to accelerate bone regeneration. Therefore, utilizing biomaterials to regulate mitophagy offers a promising avenue to accelerate ACP release and bone matrix mineralization, thereby facilitating bone regeneration [18–20].

Copper, traditionally recognized as a human body trace element involved in diverse cellular functions, possesses the ability to regulate and integrate cell biological activities in response to external stimuli. It functions as a dynamic signaling molecule and a metal allosteric regulatory factor [21,22]. The previous studies have demonstrated the antibacterial and immunomodulatory properties of copper-incorporated bioactive glasses, nanosheets, and metal implants, as well as their ability to promote angiogenesis and osteogenic differentiation [23–26]. Additionally, copper plays a crucial role in various mitochondrial functions, including energy metabolism, mitophagy, and mitochondrial dynamics. As a result, it effectively regulates cellular fate and function, even influencing cell death [27–30]. The regulation of mitochondrial dynamics and reactive oxygen species (ROS) by copper has been implicated as pivotal triggers for initiating mitophagy [31–37]. By inducing non-cytotoxic copper overload, the promotion of mitochondrial fission can elevate mitochondrial ROS (mROS) levels and enhance mitochondrial turnover [38]. Although these studies have established associations between copper and mitophagy, as well as between copper and bone regeneration, whether copper promotes bone mineralization via mitophagy has not been definitively elucidated [39–41].

Bioactive glass is widely recognized as a promising material for bone regeneration due to its remarkable biocompatibility, bioactivity, mechanical strength, and osteoinductive properties [42–44]. Notably, mesoporous bioactive glasses have emerged as effective carriers for functional ions like strontium, copper, cerium and zinc, leveraging their mesoporous structure and expansive surface area [45]. Cu-doped mesoporous bioactive glass nanoparticles (Cu-MBGNs) have demonstrated proficiency in delivering copper ion, regulating release concentrations within safe therapeutic ranges to mitigate potential toxicity [46]. Recent study has demonstrated that Cu-BG can enhance extracellular vesicles production by activating the HIF-1 signaling pathway and autophagy, thereby promoting angiogenesis and bone regeneration [47]. Therefore, the utilization of Cu-MBGNs for delivering Cu ions to enhance osteoblast mitophagy-mediated ACP release and biomineralization may represent a promising innovative approach to accelerate bone defect regeneration. In this study, autophagy gene conditional knockout mice were utilized to estimate the role of autophagy in copper-mediated bone defect repair. Based on these findings, we further demonstrated that Cu-MBGNs activate mitophagy by stimulating ROS production and simultaneously promote mitochondrial fission to reinforce mitophagy pathway, subsequently facilitating mitochondrial calcium transfer and ACP release, thereby accelerating bone mineralization and promoting defect healing.

2. Results

2.1. Synthesis and characterization of Cu-MBGNs

By utilizing the sol-gel method, Cu/L-ascorbic acid complex was employed as the copper precursor for synthesizing highly dispersed Cu-MBGNs. Fig. 1A illustrated the synthesis schematic diagram of Cu-MBGNs. The representative SEM images of Cu-MBGNs demonstrated their spherical morphology. TEM analysis further confirmed the visible mesopores within the Cu-MBGNs (Fig. 1B). The size of all particles appears to fall within the range of 100–300 nm. Their morphology aligns with particles synthesized using similar methods as reported in the literature, indicating the Cu-MBGNs' characteristics of nanoparticles possessing mesoporous [48] (Fig. 1B and C). Next, the elemental composition and valence state of Cu-MBGNs were further investigated, and representative EDS spectra were provided to confirm the presence of Si, Ca, O, and Cu within the particles (Fig. 1D). The XPS scans revealed characteristic binding energy peaks of carbon, oxygen, and copper that were consistent with the EDS findings (Fig. 1E). The Cu 2p core level spectra of Cu exhibited 4 peaks, with peak positions at approximately 935 eV corresponding to Cu $2p_{3/2}$ and 955 eV related to Cu $2p_{1/2}$, confirming that Cu^{2+} was the main oxidation state of Cu in Cu-MBGNs. Fig. 1F shows the FTIR spectra of MBGN, Cu-MBGN and ascorbic acid. The bands located at approximately 812 cm^{-1} and range of 1299-900 cm^{-1} can be attributed to the Si-O-Si symmetric stretching vibrations and asymmetric vibrations [49]. The bands of ascorbic acid located at 1754 and 1673 cm^{-1} can be attributed to the stretching vibration of C=O and C=C respectively and these spectral bands are absent in Cu-MBGNs, indicating that ascorbic acid was decomposed during the sintering process. To evaluate its biological performance, we conducted experiments on ion release and biocompatibility. Through the ion release experiment, we found that Cu-MBGNs were capable of gradually releasing calcium, silicon and copper ions (Fig. 1G). MBGNs and Cu-MBGNs were soaked in simulated body fluids (SBF) to test its biological activity, and SEM images after 3 days of mineralization showed the formation of crystals on the surface of MBGNs and Cu-MBGNs (Fig. 1H). Moreover, the FTIR spectra obtained after mineralization revealed the emergence of new spectral bands at approximately 560 and 604 cm^{-1}, corresponding to P-O bending vibrations in PO_4^{3-} (Fig. 1F), suggesting the formation of apatite crystals and no significant difference in biological activity between MBGNs and Cu-MBGNs [50]. The biocompatibility of MBGNs and Cu-MBGNs was evaluated by testing their leaching solutions with CCK8. No cytotoxicity was observed in the leaching solutions of different concentrations at 1, 3 and 5 days. Notably, the leaching solution of Cu-MBGNs at a concentration of 100 % without dilution showed stronger proliferation-promoting activity compared to MBGNs at day 3 (Fig. 1I), indicating its excellent biocompatibility. This was also verified by SEM characterization of osteoblasts, which showed no significant change in the morphology and adhesion status of osteoblasts after direct co-culture with MBGNs or Cu-MBGNs, or cultured with their conditioned medium (Fig. 1J).

2.2. Cu-MBGNs promote bone regeneration in a mouse model with femoral defect

For a comprehensive evaluation of the impact of Cu-MBGNs on bone regeneration, the mouse femur defect model was prepared for *in vivo* experiments. Blood clots laden with PBS (sham group), MBGNs, or Cu-MBGNs were placed within the defects to ensure stability against blood flow while achieving initial hemostasis. Micro-CT scans were performed at 0, 2 and 4 weeks post-surgery, followed by sacrifice at the end of the fourth week (Fig. 2A). Micro-CT analysis revealed that the Cu-MBGNs group exhibited superior and more efficient bone regeneration within the defect area compared to the sham and MBGNs groups. This was evidenced by a significant increase in parameters such as bone mineral density (BMD), bone volume ratio (BV/TV) and trabecular thickness (Tb. Th), with trabecular number (Tb. N) showed no significant difference (Fig. 2B and C). The HE and Masson staining further confirmed a significantly elevated level of new bone tissue formation in the Cu-MBGNs group (Fig. 2D and H). The immunofluorescence (IF) assay targeting $CD31^+$ and $EMCN^+$ type H vessels was performed to demonstrate the vascularization promotion capabilities of Cu-MBGNs, which are crucial for bone repair and nutrient support (Fig. 2E and I). The Cu-MBGNs group exhibited a significant increase in percentage of OCN^+ osteoblasts and osteoblast number per bone perimeter was also increased (Fig. 2F, J and K). Calcein/alizarin red S (ARS) labeling was used to observe the rate of bone mineral deposition over time, revealing heightened activity in new bone formation and mineral deposition in the Cu-MBGNs group compared to the sham and MBGNs groups (Fig. 2G and L). Collectively, these data indicate that Cu-MBGNs have the potential to enhance *in vivo* bone mineral deposition and effectively facilitate the

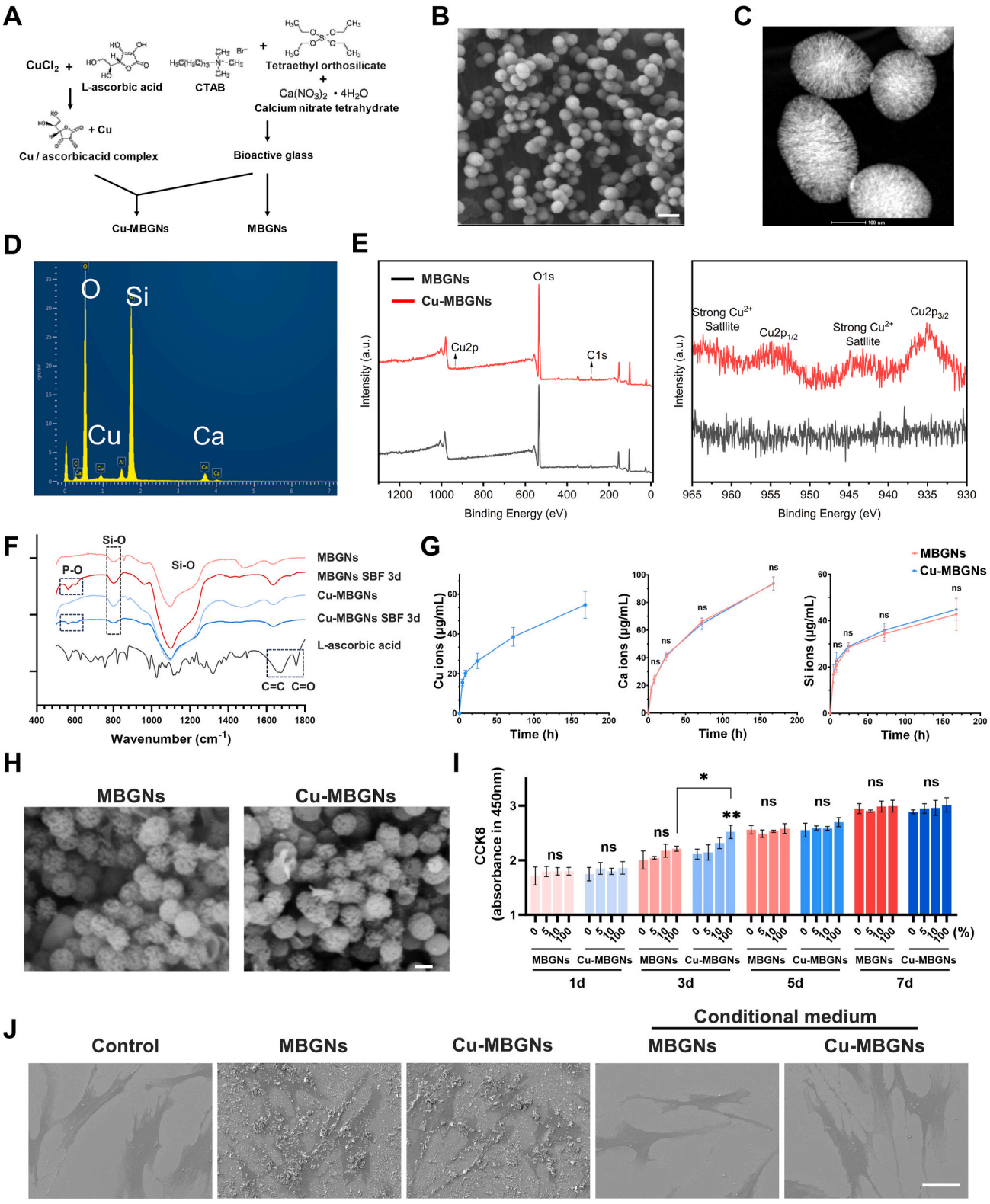

Fig. 1. Synthesis and characterization of Cu-MBGNs. **A)** Schematic diagram of the synthesis process of MBGNs and Cu-MBGNs. **B)** SEM images of Cu-MBGNs. Scale bar = 200 nm. **C)** TEM images of Cu-MBGNs. Scale bar = 100 nm. **D)** EDS spectra of Cu-MBGNs. **E)** XPS spectra of MBGNs and Cu-MBGNs and high-resolution scan of Cu $2p_{3/2}$ and Cu $2p_{1/2}$ peaks. **F)** FTIR spectra of MBGNs, Cu-MBGNs, L-ascorbic acid and MBGNs and Cu-MBGNs after immersion in SBF for 3 d. **G)** Ion release profiles of MBGNs and Cu-MBGNs in HBSS without Ca^{2+} (n = 3). **H)** Representative SEM images of MBGNs and Cu-MBGNs after immersion in SBF for 3 d. Scale bar = 100 nm. **I)** CCK8 assay results of BMSCs cultured with the dissolution products of MBGN and Cu-MBGNs with different dilution ratio for 1, 3 and 5 days. **J)** Representative SEM images of osteoblasts' morphology treated with MBGNs, Cu-MBGNs or conditioned medium from MBGNs or Cu-MBGNs for 6 h. Scale bar = 50 μm $^{*}p < 0.05$, $^{**}p < 0.01$, ns $p > 0.05$.

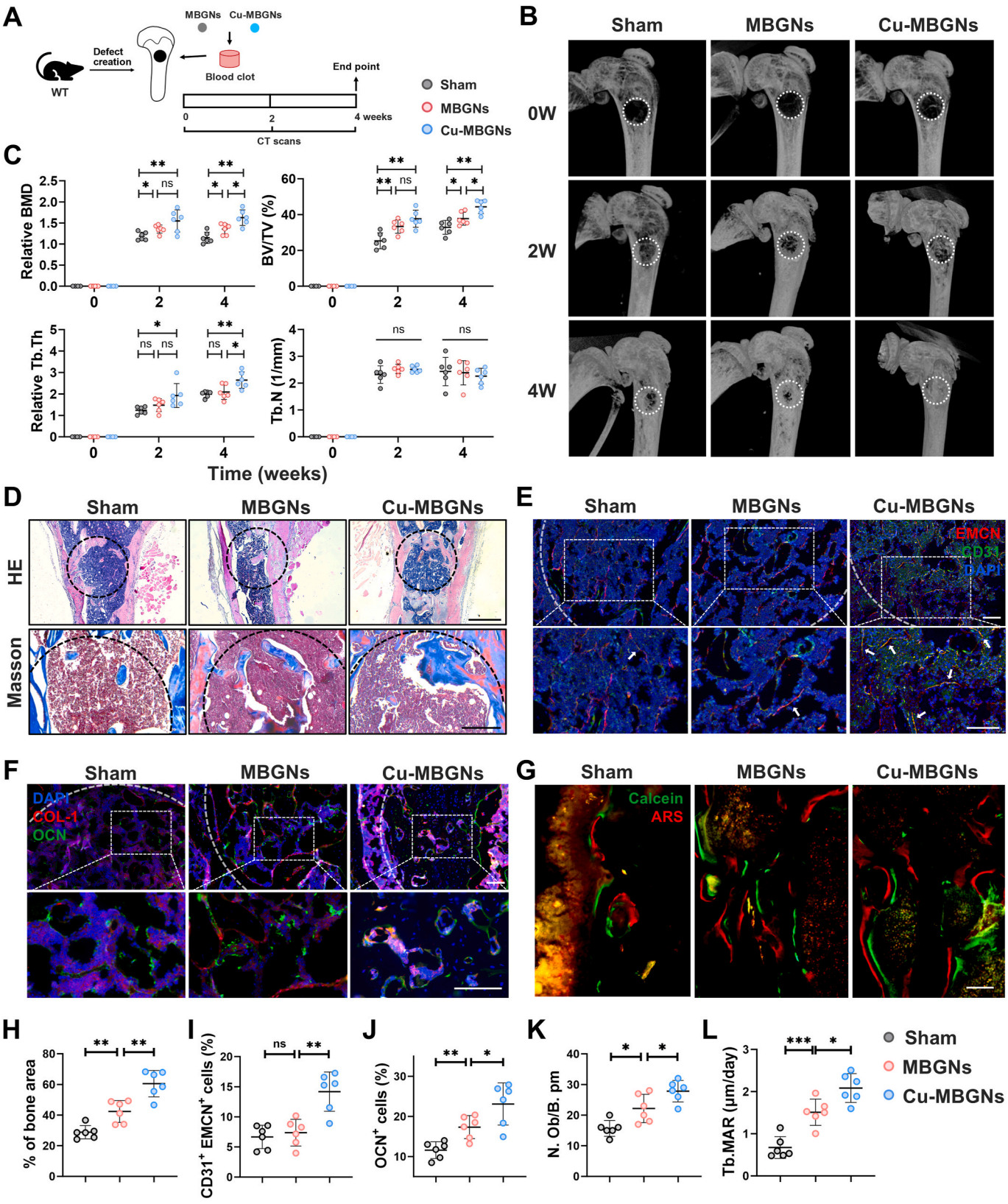

Fig. 2. Cu-MBGNs promote bone regeneration *in vivo*. **A)** Schematic diagram of mouse femoral defect model construction and MBGNs or Cu-MBGNs treatment. **B)** Representative micro-CT reconstruction images of femoral defect at 0, 2 and 4 weeks. **C)** The measurements of relative BMD, BV/TV, Tb. N and relative Tb. Th of femoral defects at 0, 2 and 4 weeks. **D)** Representative H&E and Masson staining images of the femoral defects in sham, MBGNs and Cu-MBGNs groups at 4 weeks. Scale bar = 500 μm in H&E and 200 μm in Masson. **E)** Representative IF images of H type vessels (marked by white arrows) within femoral defects at 4 weeks, scale bars = 50 μm. **F)** Representative IF images of OCN^+ and $COL\text{-}1^+$ cells within femoral defects at 4 weeks, scale bars = 100 μm. **G)** Representative images of calcein/ARS labeling for bone mineralization within the 4th week after surgery, scale bar = 50 μm. **H-L)** Semi-quantitative analyses correspond to D, E, F, G. $^*p < 0.05$, $^{**}p < 0.01$, $^{***}p < 0.001$, ns $p > 0.05$, n = 6 individuals for each group.

healing of bone defects.

2.3. Cu-MBGNs promote bone defect repair depending on osteoblast autophagy

The favorable bone regeneration potential of Cu-MBGNs prompted a comprehensive investigation into the role of autophagy in this process. Specifically, mice with conditional knockout (CKO) of autophagy gene 5 (*Atg5*) in osteogenic lineage cells (*Prx1-cre; Atg5$^{f/f}$* mice) by Cre/LoxP system were selected for further analysis, while *Atg5$^{f/f}$* mice served as the control group (Fig. 3A). The activation of autophagy by Cu-MBGNs and the blockade of autophagy after *Atg5* knockout were demonstrated through immunofluorescence staining of autophagy substrate p62 and autophagy marker microtubule-associated protein light chain 3 (LC3) (Fig. S1). The micro-CT analysis revealed that the knockout of *Atg5* in osteoblasts markedly hindered the bone regeneration efficacy of MBGNs and Cu-MBGNs (Fig. 3B and C). The BMD, BV/TV and Tb. N of *Prx1-cre; Atg5$^{f/f}$* mice treated with MBGNs and Cu-MBGNs were significantly reduced compared to those of *Atg5$^{f/f}$* mice receiving the same treatment at 2- and 4-week post-surgery (Fig. 3C). Remarkably, the superior effect on promoting bone regeneration observed with Cu-MBGNs compared to MBGNs in *Atg5$^{f/f}$* mice was completely abolished in CKO mice (Fig. 3C). The histological analysis revealed that the deficiency of *Atg5* was responsible for the compromised ability of Cu-MBGNs to promote bone regeneration (Fig. 3D). Meanwhile, the percentage and number of COL-1^{+} and OCN^{+} cells per bone perimeter decreased in CKO group treated with Cu-MBGNs (Fig. 3E). Fluorochrome labeling using Calcein/ARS also revealed impaired mineralization of bone defects attributed to inhibited autophagy in osteoblasts (Fig. 3F). The findings imply that autophagy plays a pivotal role in Cu-MBGNs-induced bone regeneration.

2.4. Cu-MBGNs promote mitophagy and release of ACP in osteoblasts

Considering the crucial role of autophagy in Cu-MBGNs-mediated bone repair and the significant impact of mitophagy on ACP release, the investigation further focuses on the impact of Cu-MBGNs on mitophagy in osteoblasts. After being induced with osteogenic induction medium for 1 week, the osteoblasts derived from bone marrow mesenchymal stem cells (BMSCs) were exposed to varying concentrations of conditioned medium to discern the ion-related effects on *in vitro* mineralization for an additional 2 weeks. The increase in concentration of MBGNs' conditioned medium significantly enhances mineralization, reaching a plateau at a concentration of 5 %. Notably, Cu-MBGNs facilitated mineralization across the concentration ranged from 0.2 to 20 %; however, their effectiveness started to diminish when the concentration went beyond 10 % (Fig. 4A). At the 5 % concentration, Cu-MBGNs displayed superior promotion of mineralization compared to MBGNs (Fig. 4A). The mineralization-promoting ability of Cu-MBGNs was confirmed by subsequent *in vitro* assays, which justified further analysis at this concentration. Matrix vesicles (MVs), serving as carriers for osteoblasts to transport ACP to collagen fibers, were isolated to assess the secreted ACP content by osteoblasts. TEM assessments revealed no significant differences in the morphology or size of MVs among control, MBGNs, and Cu-MBGNs groups (Fig. 4B). The digestion of MVs with hydrochloric acid, followed by analysis of calcium content, demonstrated an enhanced secretion of ACP by both MBGNs and Cu-MBGNs, with Cu-MBGNs exhibiting a more pronounced effect (Fig. 4B). Additionally, the influence of Cu-MBGNs on osteoblast mitophagy was investigated, highlighting its crucial role in ACP secretion. To determine the duration of maximal activation of osteoblast autophagy following Cu-MBGNs stimulation, we assessed the conversion levels of LC3B-I to LC3B-II and the content of autophagic substrate p62 at 6, 12, and 24 h after introducing conditioned media. Furthermore, we confirmed changes in autophagy flux by inhibiting it with bafilomycin A1 (Baf A1). The Western blot results demonstrated a significant induction of autophagy flux at 6 h and the Cu-MBGNs group exhibited higher levels of autophagy activity; moreover, following the addition of Baf A1, the LC3B-II content in the MBGNs and Cu-MBGNs groups increased further, indicating a rise in the conversion from LC3B-I to LC3B-II, rather than an accumulation of LC3B-II due to autophagy inhibition. Therefore, this time point was selected as the duration for subsequent investigations into autophagy induction (Fig. 4C). The subsequent colocalization studies of mitochondria and lysosomes using Mito-tracker and Lyso-tracker demonstrated significantly higher levels of colocalization in the Cu-MBGNs group compared to both the control group and MBGNs (Fig. 4D), suggesting Cu-MBGNs' stimulatory effect on osteoblast mitophagy. Moreover, TEM observations revealed an elevated quantity of autophagosomes and mitochondria enveloped by autophagosomes following Cu-MBGN treatment, providing further validation of its impact on mitophagy (Fig. 4E). The mitochondrial Ca^{2+} fluorescence probe, Rhod-2, was employed to assess the levels of mitochondrial calcium, recognizing the potential of ACP to induce mitophagy through Ca^{2+} overload. Fig. 4F demonstrated a reduction in mitochondrial Ca^{2+} accumulation following Cu-MBGN treatment, suggesting the potential of Cu-MBGNs to enhance mitochondrial Ca^{2+} transport. Meanwhile, the total intracellular Ca^{2+} probe Fluo-3 was employed to assess Ca^{2+} levels in osteoblasts stimulated by MBGNs or Cu-MBGNs. The results indicated that intracellular Ca^{2+} levels were significantly reduced in the Cu-MBGNs group (Fig. S2A). These findings suggest that copper may activate mitophagy in osteoblasts and reduce mitochondrial calcium accumulation that promotes ACP transfer to matrix vesicles, which are subsequently released into the extracellular space. In addition, to further validate the role of copper ions in promoting mitophagy in Cu-MBGNs, we employed a culture medium containing 20 μM $CuCl_2$ as a positive control, alongside MBGNs as a negative control in the aforementioned experiment. The colocalization experiment of mitochondria and lysosomes showed that $CuCl_2$ has a similar effect of Cu-MBGNs on promoting mitophagy (Fig. S2B). The ARS experiment also demonstrated that $CuCl_2$ promoted osteoblast mineralization, but its effect was weaker than that of Cu-MBGNs (Fig. S2C).

2.5. Cu-MBGNs promote mitophagy by recruiting PINK1/Parkin

The above study has revealed that Cu-MBGNs exhibits the potential to mitigate mitochondrial calcium accumulation by inducing mitophagy in osteoblasts. Therefore, a comprehensive investigation was conducted to elucidate the precise mechanism underlying the initiation of Cu-MBGNs-induced mitophagy in osteoblasts. Considering the strong correlation between the reduction in mitochondrial membrane potential (MMP), depolarization, and initiation of mitophagy, we conducted an in-depth investigation into the PINK1/Parkin pathway for activating mitophagy. Through isolation of cytoplasmic and mitochondrial proteins, our WB analysis revealed a notable enrichment of PINK1/Parkin, LC3B-I/II and LAMP2A (a marker protein for lysosomes) on mitochondria following treatment with Cu-MBGNs. This finding was further supported by IF colocalization analysis demonstrating the presence of PINK1 on mitochondria. (Fig. 5A and B). Similarly, IF staining on femoral defects treated with Cu-MBGNs revealed an increased colocalization of PINK1 with mitochondria, marked by TOM20 (Fig. S3A). Meanwhile, $CuCl_2$ treatment also demonstrated the increased colocalization between PINK1 and mitochondria (Fig. S3B and F). The tetramethylrhodamine methyl ester (TMRM) was employed to evaluate MMP levels due to the induction of mitochondrial depolarization by MMP reduction is the initiating factor for PINK1 recruitment and stabilization on mitochondria. We used a membrane-impermeable calcium binding fluorescent probe, calcein blue, to image the formation of intracellular ACP [11]. Simultaneous assessment of MMP using TMRM, Mito-tracker Green and calcein blue aimed to investigate the regulatory effect of Cu-MBGNs on ACP transport in mitochondria depleted or depolarized in terms of MMP. Cu-MBGNs led to a decrease in MMP and an increase in the colocalization of calcein and depolarized mitochondria (Fig. 5C). Furthermore, cyclosporin A (CsA), a mitophagy inhibitor, was employed

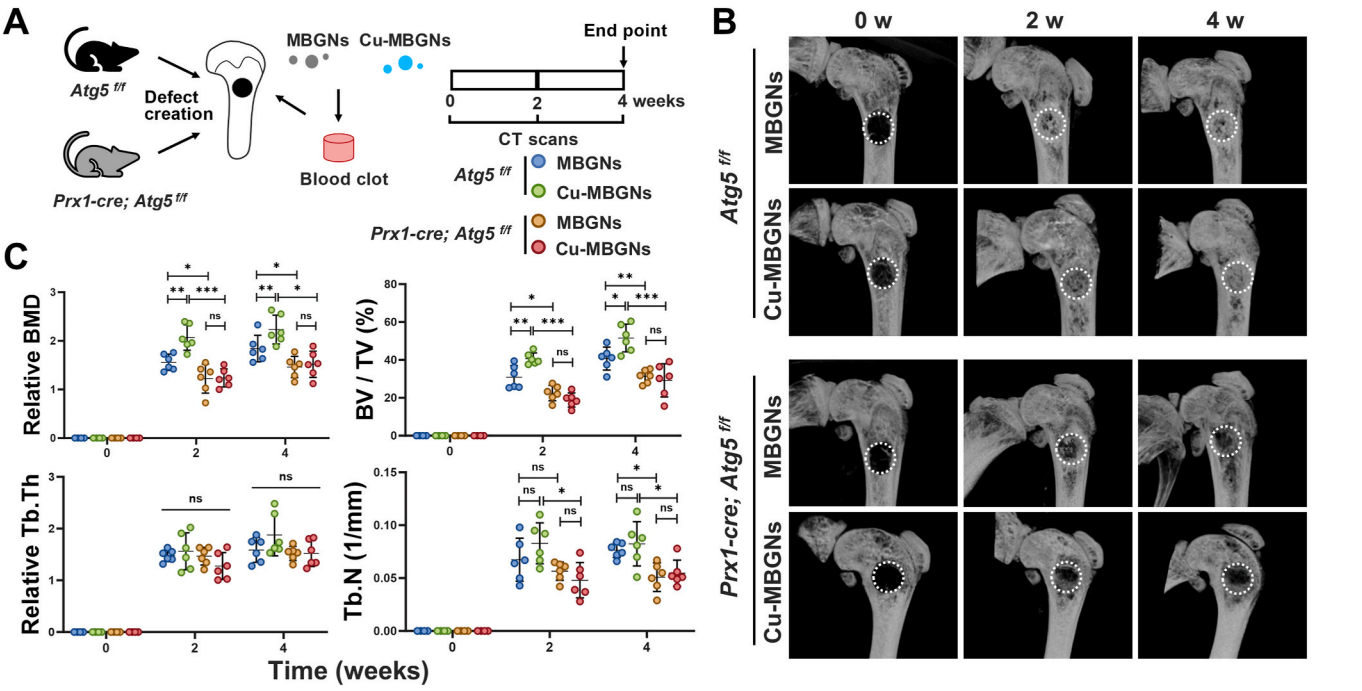

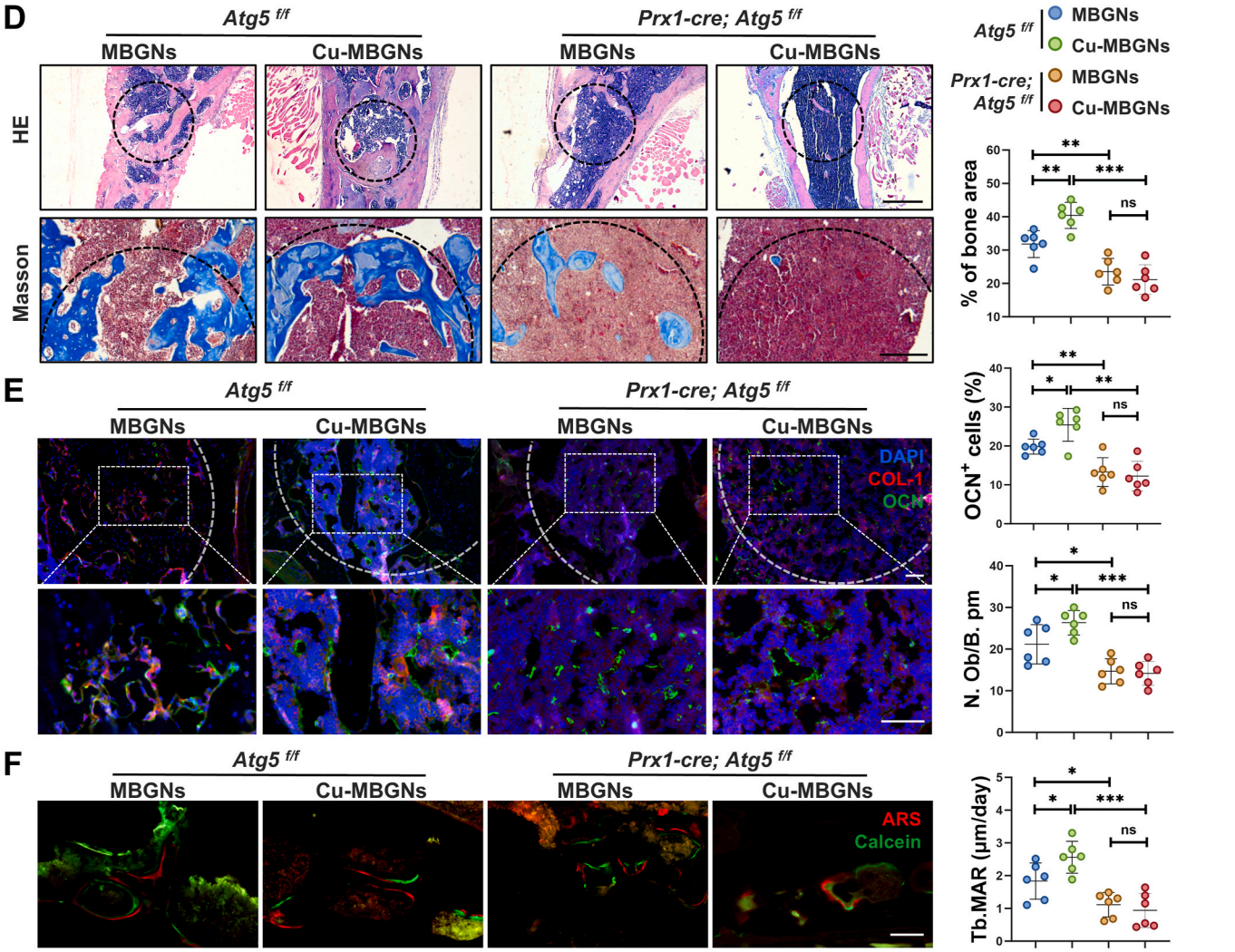

(caption on next page)

Fig. 3. Cu-MBGNs promoted bone defect repair promotes bone defect repair depending on osteoblast autophagy. **A)** Schematic diagram of femoral defect model construction and MBGNs or Cu-MBGNs treatment on *Atg5*$^{f/f}$ and *Prx1-cre; Atg5*$^{f/f}$ mice. **B)** Representative micro-CT images of femoral defect on *Atg5*$^{f/f}$ and *Prx1-cre; Atg5*$^{f/f}$ mice treated with MBGNs or Cu-MBGNs at 0, 2 and 4 weeks. **C)** The measurements of relative BMD, BV/TV, Tb. N and Tb. Th of femoral defects on *Atg5*$^{f/f}$ and *Prx1-cre; Atg5*$^{f/f}$ mice treated with MBGNs or Cu-MBGNs at 0, 2 and 4 weeks. **D)** Representative H&E and Masson staining images and percentage of bone area of the femoral defects on *Atg5*$^{f/f}$ and *Prx1-cre; Atg5*$^{f/f}$ mice treated with MBGNs or Cu-MBGNs at 4 weeks. Scale bar = 500 μm in H&E and 200 μm in Masson **E)** Representative immunofluorescent images and percentage of OCN^{+} osteoblasts and COL-1^{+} bone trabeculae within femoral defects on *Atg5*$^{f/f}$ and *Prx1-cre; Atg5*$^{f/f}$ mice treated with MBGNs or Cu-MBGNs at 4 weeks and the number of osteoblast number per bone perimeter. Scale bars = 100 μm. **F)** Representative images of calcein/ARS labeling for bone mineralization and the trabecular mineralization apposition rate on *Atg5*$^{f/f}$ and *Prx1-cre; Atg5*$^{f/f}$ mice treated with MBGNs or Cu-MBGNs within the 4th week after surgery. $^{*}p < 0.05$, $^{**}p < 0.01$, $^{***}p < 0.001$, ns $p > 0.05$, n = 6 individuals for each group.

to investigate the impact of Cu-MBGNs on mitophagy in osteoblasts. The inhibition of mitochondrial permeability by CsA impeded the ability of Cu-MBGNs to reduce MMP levels, resulting in a decrease in ACP formation (Fig. S3C and G). The results from TEM, WB, IF, and colocalization analyses also demonstrated that CsA effectively counteracted the Cu-MBGN-induced enhancement of mitophagy (Fig. 5D, E, F and Fig. S3D&H). The mitochondrial calcium probe revealed an increase in mitochondrial calcium accumulation following treatment with CsA (Fig. S3E and I). The analysis of the calcium content in MV and ARS revealed that CsA stimulation inhibited the potentiation of Cu-MBGNs on ACP release (Fig. 5G and H). In conclusion, it can be inferred that Cu-MBGNs enhance the release of ACP by reducing osteoblast MMP activity, promoting mitophagy, and facilitating ACP transportation within mitochondria (Fig. 5I).

2.6. Cu-MBGNs triggers mitophagy through binding with glutathione to increase mROS levels

The ability of copper to bind glutathione (GSH) leads to the initiation of oxidative stress. Additionally, its metabolite, mROS, plays a crucial role as a metabolic regulator and contributes significantly to maintaining mitochondrial quality control. Hence, we conducted an in-depth investigation into the potential involvement of Cu-MBGNs in regulating oxidative stress and their impact on inducing mitophagy in osteoblasts to elucidate the mechanism underlying mitophagy activation. The levels of reduced glutathione in osteoblasts treated with Cu-MBGNs for 6 h were observed to be lower compared to both the control group and the MBGNs group (Fig. 6A). Additional analysis using MitoSOX revealed that Cu-MBGNs significantly enhanced mROS accumulation (Fig. 6B). This observation suggests that the binding of GSH may lead to an increase in mROS production, thereby challenging the antioxidant capacity of osteoblasts and triggering oxidative stress. However, measurements of ATP content indicated that Cu-MBGNs treatment had no significant effect on ATP generation in osteoblasts (Fig. S4A). This suggests that the increased mROS remain within a physiological range and may be effectively cleared through mitophagy, thereby preserving cellular energy metabolism and overall cell health. After mitigating oxidative stress with N-Acetylcysteine (NAC), we observed an increase in mitochondrial calcium accumulation, MMP levels, and a decrease in ACP levels (Fig. 6C, D and S4B), indicating Cu-MBGNs' ability to reduce MMP and transport through oxidative stress. The Western blot, IF, and colocalization analysis showed that NAC effectively counteracted the impact of Cu-MBGNs on enhancing mitophagy (Fig. 6E, F, G and S4C). The NAC treatment significantly inhibited the Cu-MBGNs' ability to enhance ACP release, as evidenced by the evaluation of calcium content in MV and ARS (Fig. 6H and S4D). The findings imply that Cu-MBGNs promote mitophagy and enhance the transport of mitochondrial ACP by elevating osteoblast mROS levels, inducing oxidative stress and quality control in mitochondria, thereby initiating mineralization.

2.7. Cu-MBGNs induce mitophagy by enhancing the process of mitochondrial fission

Considering the pivotal role of mitochondrial dynamics in initiating mitophagy, we investigated whether Cu-MBGNs can modulate mitophagy by influencing mitochondrial dynamics. Dynamin related protein 1 (Drp1) governs the process of mitochondrial fission and exerts shear effects on the mitochondrial membrane through recruitment onto mitochondria. Initially, IF was employed to assess the subcellular localization of Drp1 on mitochondria, revealing a significantly enhanced co-localization between Drp1 and mitochondria in the Cu-MBGNs group (Fig. 7A). The analysis of mitochondrial morphology indicated a significant reduction in the proportion of cells exhibiting hyperfused mitochondria and an increase in intermediate mitochondria in the presence of Cu-MBGNs (Fig. 7B). These findings imply that Cu-MBGNs have the potential to induce mitochondrial fission. To further investigate the regulatory role of Cu-MBGNs in mitophagy through mitochondrial dynamics, we employed Mdivi-1 as a GTPase activity inhibitor of Drp1 to inhibit mitochondrial division. Subsequent analysis of mitochondrial morphology revealed an increased proportion of cells with excessively fused mitochondria upon introduction of Mdivi, indicating that the function of Cu-MBGNs in promoting mitochondrial fission was hindered (Fig. S5A). Furthermore, we examined the impact of mitochondrial dynamics disruption on Cu-MBGNs-induced mitophagy, and observed that the inhibition of mitochondrial fission using Mdivi resulted in enhanced accumulation of mitochondrial calcium, preservation of MMP, and decreased ACP levels (Fig. 7C, D and S5B), revealing the influence of Cu-MBGNs on reducing MMP and facilitating ACP transport through mitochondrial dynamics. The Western blot, IF, and colocalization analysis demonstrated that Mdivi effectively counteracted the enhancement of mitophagy caused by Cu-MBGNs (Fig. 7E, F and S5C). The administration of Mdivi notably inhibited the increase in ACP release from Cu-MBGNs, as evidenced by the assessment of calcium content in MV and ARS (Fig. 7G and H). The findings indicate that Cu-MBGNs enhance mitophagy and facilitate the transport of mitochondrial ACP by modulating mitochondrial dynamics and promoting mitochondrial fission, thereby establishing a foundation for maintaining mitochondrial quality control and ultimately initiating mineralization.

3. Discussion

Several studies have provided evidence that copper can promote osteogenic differentiation to facilitate bone regeneration [51–53], but little is known about copper's involvement in biomineralization during this process. In this study, using osteoblast-specific *Atg5* knockout mouse models and mitochondrial function experiments, we demonstrated that Cu-MBGNs enhanced osteoblast mitophagy by inducing ROS production and simultaneously promoting mitochondrial fission to further reinforce mitophagy pathway. In this study, Cu-MBGNs facilitated mitochondrial calcium transfer and ACP release, ultimately expediting bone biomineralization and defect repair.

The process of bone healing can be delineated into three distinct stages: inflammation, repair, and remodeling. During the initial inflammatory stage, immune cells infiltrate the injured area, and new blood vessels begin to form. Inflammatory mediators present at the injury site facilitate the migration of bone progenitor cells, which subsequently undergo differentiation into osteoblasts. These osteoblasts play a pivotal role by synthesizing extracellular matrix proteins and mineralizing them with ACP, thereby facilitating the deposition and organization of new bone tissue [4,5]. Copper ions within an appropriate concentration range can promote cellular migration, adhesion, and osteogenic differentiation [52,54]. The presence of elevated levels

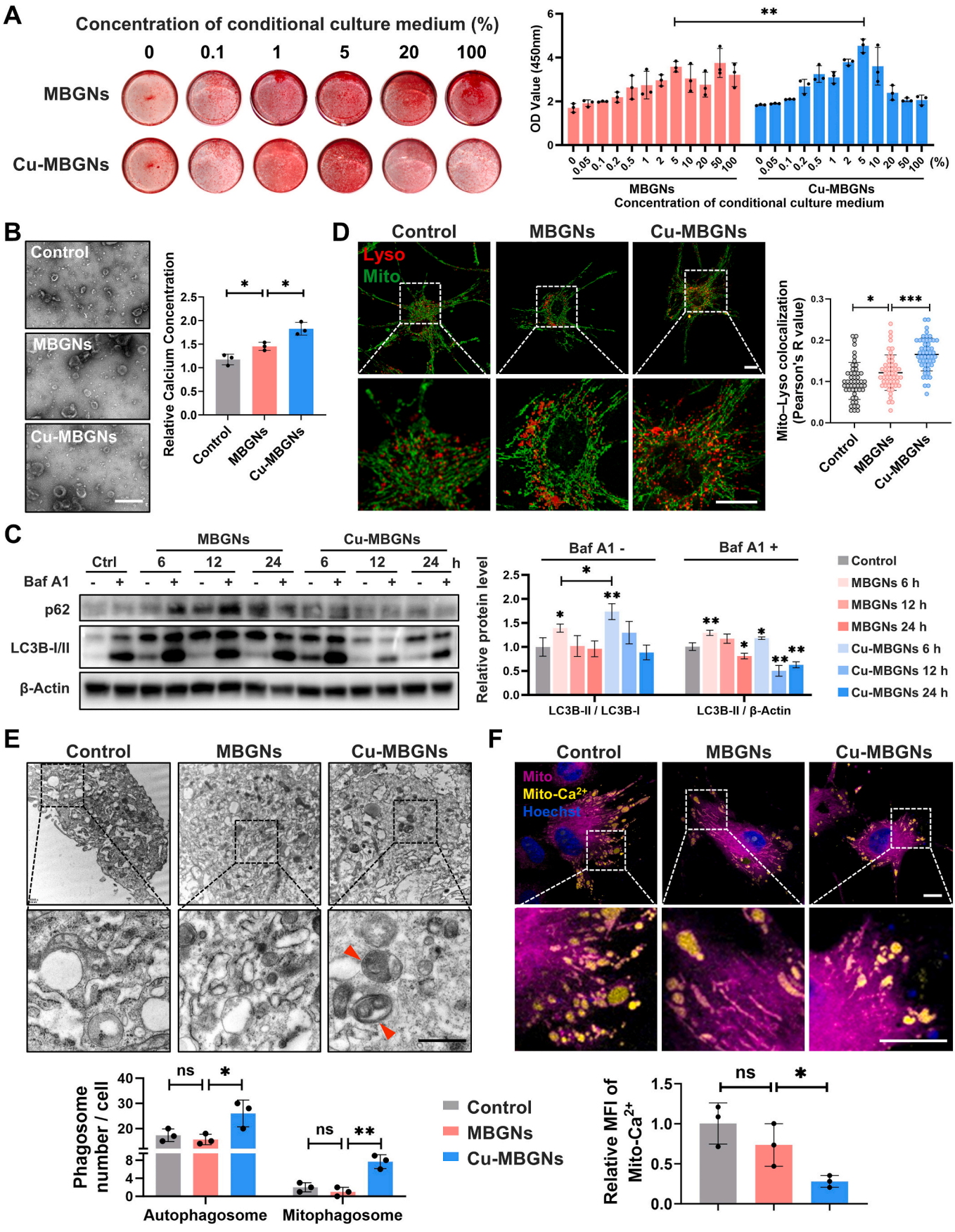

(caption on next page)

Fig. 4. Cu-MBGNs promote mitophagy and release of ACP in osteoblasts. **A)** ARS staining and quantitative analysis of mineralized nodules of osteoblasts treated with conditioned medium from MBGNs or Cu-MBGNs (n = 3). **B)** Representative TEM images and calcium concentration of MVs isolated from osteoblasts treated with conditioned medium from MBGNs or Cu-MBGNs for 1 week (n = 3). Scale bar = 500 nm. **C)** Representative images of WB of autophagy flux and relative level of LC3B-II/LC3B-I or LC3B-II of osteoblasts treated with conditioned medium from MBGNs or Cu-MBGNs for 6, 12 and 24 h, with or without Baf A1 (n = 3). **D)** Representative images of live cell imaging and colocalization coefficient (Pearson's R value) of mitochondria and lysosomes in osteoblasts treated with conditioned medium from MBGNs or Cu-MBGNs for 6 h (n = 50). Scale bars = 10 μm. **E)** Representative TEM images of autophagosome and mitophagosome (marked by red arrows) and the number of them in osteoblasts treated with conditioned medium from MBGNs or Cu-MBGNs for 6 h (n = 3). Scale bars = 1 μm. **F)** Representative images of mitochondria and mitochondrial Ca^{2+} in osteoblasts treated with conditioned medium from MBGNs or Cu-MBGNs for 6 h and the mean fluorescence intensity (MFI) of Rhod-2 (n = 3). Scale bars = 10 μm $^{*}p < 0.05$, $^{**}p < 0.01$, $^{***}p < 0.001$, ns $p > 0.05$.

of copper ions, however, demonstrates cytotoxicity and no longer exerts a stimulatory effect on the process of osteogenic differentiation [24], which aligns with our finding (Fig. 3A). Therefore, it is imperative to elucidate the bidirectional mechanism of copper on osteoblasts, especially considering the increasing utilization of copper-based materials.

When examined as a toxic heavy metal, copper exposure has been shown to induce autophagy by upregulating the expression of autophagy-related genes such as ATG5, SQSTM1, and LC3, while also inducing oxidative stress [55,56]. Autophagy is a conserved biological process in eukaryotic organisms that maintains cellular homeostasis in response to nutrient deprivation or other stress conditions by degrading and recycling cellular components [57,58]. Furthermore, recent investigations have highlighted the pivotal role of mitochondria in cellular copper metabolism and homeostasis, including copper's regulation of mitochondrial function, cellular plasticity, and induction of cell death dependent on mitochondrial respiration [29,59,60]. Mitophagy, the selective autophagy of damaged mitochondria, is crucial for maintaining mitochondrial quality. The activation of mitophagy in various cell types by copper has been observed, indicating its role as a protective response to mitochondrial damage [40,41]. However, the effect of appropriate concentrations of copper on autophagy or mitophagy in osteoblasts have not been thoroughly explored. To address this, we utilized *Prx1-cre; Atg5$^{f/f}$* mice as models with specific autophagy defects in osteogenic lineage-committed cells. Our findings demonstrate that the osteogenic effect of Cu-MBGNs was nullified in these mice, indicating that autophagic activity in osteogenic lineage cells is a primary target for Cu-induced bone healing. These findings align with previous studies that support copper's ability to enhance autophagy [55,61].

Given the inherently slow pace of natural bone mineralization, enhancing the rate of mineralization by osteoblasts within the extracellular matrix presents a promising therapeutic approach alongside promoting osteogenic differentiation. As a precursor for bone hydroxyapatite, ACP serves as a vital raw material for bone mineralization [62]. Some studies indicate that enhancing mitophagy can maintain cellular homeostasis by removing damaged mitochondria [63]; and mitophagy plays a crucial role in the synthesis and intracellular transport of ACP [9,10]. The initiation of PINK1/Parkin dependent mitophagy primarily occurs due to mitochondrial membrane potential loss raised from ACP accumulating in mitochondria [10,64]. PINK1 stabilizes and accumulates on mitochondria, selectively recruits Parkin to aggregate into mitochondria, mediates mitochondrial ubiquitination, binds to autophagy receptor proteins, is then encapsulated by autophagosomes, and finally fuses with lysosomes, transferring ACP to ECM through MV [10,65,66]. Therefore, utilizing the impact of Cu-MBGNs on mitophagy and ACP secretion is essential for studying accelerating bone mineralization. Through intracellular and mitochondrial Ca^{2+} detection, we found that Cu-MBGNs treatment resulted in a decrease in Ca^{2+} concentration. This decrease may be associated with the formation of ACP in mitochondria, where calcium phosphate cannot be labeled effectively by Ca^{2+} probes, consistent with the findings of Tang et al. [9]. In the present study, Cu-MBGNs treatment decreased mitochondrial membrane potential, reduced mitochondrial calcium accumulation, increased mineral particle formation, and increased mitophagy and autophagic flux in osteoblasts, suggesting that activating mitophagy can promote the transfer of ACP from mitochondria to matrix vesicles in osteoblasts.

Studies have shown that copper deficiency can promote glycolysis and cell proliferation, while non-cytotoxic copper overload induces oxidation and cell differentiation, with ROS production and changes in mitochondrial metabolic state playing crucial roles [35,38]. Given ROS can initiate mitophagy and copper can bind glutathione to promote ROS generation [67], we explored whether this pathway is one of the mechanisms by which Cu-MBGNs activates mitophagy. Our findings also support this perspective by demonstrating that Cu-MBGNs can trigger mitophagy, ACP transport, and mineralization through the generation of ROS. Furthermore, the production and clearance of these ROS are regulated without disrupting cellular energy synthesis and homeostasis.

The mitochondrial life cycle involves two dynamic processes, fission and fusion, collectively known as mitochondrial dynamics. Mitochondrial fission, primarily mediated by Drp1, tightens and severs the mitochondrial membrane, splitting a mitochondrion into two daughter mitochondria [68,69]. This process is a critical component of mitochondrial quality control, isolating and recycling damaged mitochondria. Recent studies have indicated that the division of peripheral regions of mitochondria enables the segregation of damaged mitochondrial components into smaller mitochondria, which are then cleared by mitophagy. These smaller mitochondria typically exhibit decreased MMP and proton dynamics, along with increased levels of ROS and Ca^{2+} before division [70]. Studies have also shown that copper deficiency can lead to mitochondrial fusion, while copper exposure increases mitochondrial fission [30,41,71,72]. Our study also demonstrated that Cu-MBGNs increased mitochondrial fission in osteoblasts. Through Mdivi to inhibit the GTPase activity of Drp1 and then block its mitochondrial fission function, we verified that Cu-MBGNs can also regulate mitophagy through mitochondrial dynamics.

Bioactive glass exhibits high biodegradability and releases a variety of ions, with calcium and silicon ions being the primary components responsible for biological activity. Calcium ions induce the proliferation, differentiation, and extracellular matrix mineralization of osteoblasts, while silicon ions contribute to hydroxyapatite precipitation and angiogenesis [73,74]. In our study, Cu-MBGNs also demonstrate the ability to release calcium and silicon ions in addition to copper ions, promoting apatite formation. These properties are similar to those of MBGNs. Consequently, MBGNs are utilized as controls in this study to investigate and highlight the role of copper in Cu-MBGNs both *in vitro* and *in vivo*. Meanwhile, the regulatory effect of copper on mitochondrial autophagy in Cu-MBGNs was further validated by the addition of copper ions alone by $CuCl_2$.

Given that natural bone defect healing requires a prolonged period to achieve complete mineralization, our study reveals the potential of Cu-MBGNs as a therapeutic strategy for promoting MVs mediated ACP secretion through mitophagy and mitochondrial dynamics, accelerating the mineralization and maturation of bone defects, restoring biomechanical function, and ultimately achieving complete healing (Fig. 8).

4. Materials and methods

4.1. Synthesis and characterization of Cu-MBGNs

Cu/L-ascorbic acid complex and Cu-MBGNs were synthesized according to previous studies [46]. Briefly, 50 mL of 0.2 M $CuCl_2{\cdot}2H_2O$ aqueous solution was heated to 80 °C under magnetic stirring for 1h, then 50 mL of 0.4 M L-ascorbic acid was added in dropwise. After further

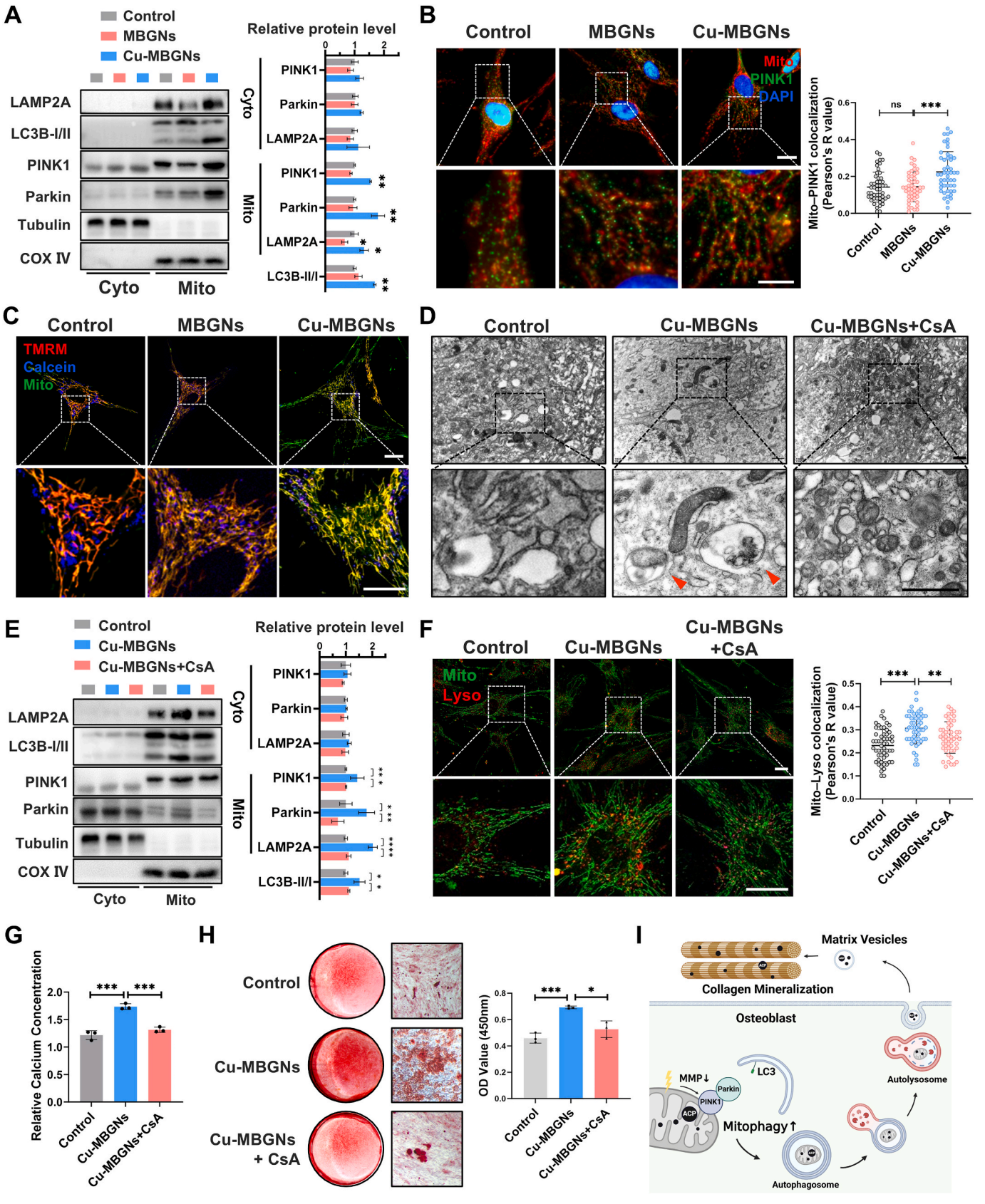

(caption on next page)

Fig. 5. Cu-MBGNs promote mitophagy by recruiting PINK1/Parkin. **A)** WB images and relative level of mitophagy related proteins in cytoplasm and mitochondria of osteoblast treated with conditioned medium from MBGNs or Cu-MBGNs for 6 h (n = 3). **B)** Representative IF images and colocalization coefficient (Pearson's R value) of PINK1 and mitochondria in osteoblasts treated with conditioned medium from MBGNs or Cu-MBGNs for 6 h (n = 50). Scale bar = 10 μm and 5 μm (enlarged figures). **C)** Representative images of live cell imaging of mitochondria, MMP (TMRM) and ACP (Calcein blue) in osteoblasts treated with conditioned medium from MBGNs or Cu-MBGNs for 6 h. Scale bar = 10 μm and 5 μm (enlarged figures). **D)** Representative TEM images of autophagosomes (marked by red arrows) in osteoblasts treated with conditioned medium of Cu-MBGNs with or without CsA for 6 h. Arrows indicate mitochondria in autophagosomes. Scale bars = 1 μm. **E)** WB images and relative level of mitophagy related proteins in cytoplasm and mitochondria of osteoblast treated with conditioned medium of Cu-MBGNs with or without CsA for 6 h (n = 3). **F)** Live cell imaging and colocalization coefficient (Pearson's R value) of mitochondria and lysosomes in osteoblasts treated with conditioned medium of Cu-MBGNs with or without CsA for 6 h. Scale bars = 10 μm (n = 50). **G)** Calcium concentration of MV isolated from osteoblasts treated with conditioned medium of Cu-MBGNs with or without CsA for 1 week (n = 3). **H)** ARS staining and quantitative analysis of mineralized nodules of osteoblasts treated with conditioned medium of Cu-MBGNs with or without CsA for 2 weeks (n = 3). **I)** Schematic illustration of mechanism of mitophagy mediated secretion of ACP. $^{*}p < 0.05$, $^{**}p < 0.01$, $^{***}p < 0.001$, ns $p > 0.05$.

reacted at 80 °C for 24 h under stirring, in order to remove precipitates and large clusters, the mixture was centrifuged at 7000 rpm for 20 min and the supernatant containing Cu/ascorbic acid complex suspension was collected.

Eight mL of ethyl acetate was added to 26 mL of deionized water dissolving 0.56 g of cetrimonium bromide (CTAB) when CTAB was completely dissolved. After 30 min of reaction under stirring, 5.6 mL 1 M ammonia solution was added for another 15 min of reaction. Then 2.88 mL of tetraethyl orthosilicate was added in, followed with 1.83 g of calcium nitrate tetrahydrate after 30min. After added with 2 mL Cu/L-ascorbic acid complex, the mixture was stirred for 4h of reaction. Then the mixture was centrifuged at 7197 RCF for 20 min to collect the formed colloid and the precipitate was washed with deionized water twice and with ethanol once. After dried at 60 °C for overnight, the collected precipitate was then calcined at 700 °C for 4 h to obtain Cu-MBGNs.

The morphology of Cu-MBGNs was examined with field emission scanning electron microscopy (FE-SEM, Carl Zeiss) at an accelerating voltage of 2 kV. Probe Cs-corrected scanning transmission electron microscopy (STEM, FEI) was used observe the microstructure. Additionally, the element composition of Cu-MBGNs was characterized via energy dispersive X-ray (EDX) analysis (X-Max^{N}, Oxford Instruments) during SEM observations. High-resolution X-ray photoelectron spectroscopy (XPS) spectra of the samples were obtained using a Thermo Scientific ESCALAB QXi spectrometer to evaluate the atomic valence state. Fourier transform infrared spectroscopy (FTIR, Nicolet 6700, Thermo Fisher Scientific) was conducted on MBGNs, Cu-MBGNs and ascorbic acid. After combined with KBr, the particles were and pressed into pellets at a weight ratio of 1:100 for analysis.

4.2. In vitro apatite formation

The *in vitro* apatite-forming ability of Cu-MBGNs was assessed by immersing the particles in simulated body fluid (SBF). Specifically, the particles were immersed in SBF at a concentration of 1 mg/mL and incubated in a shaking incubator at 37 °C with a speed of 90 rpm for up to 3 days. Then the particles were retrieved, rinsed with acetone, and dried overnight at 60 °C. Subsequently, the formation of apatite on the particles was characterized using SEM and FTIR.

4.3. Ion release of Cu-MBGNs

In summary, 10 mg of MBGN and Cu-MBGNs were immersed in 10 mL of Hank's balanced salt solution (HBSS) without Ca^{2+} and placed in an incubator at 37 °C, shaking at 90 rpm for a maximum duration of 7 days. At specified time intervals, the samples were centrifuged at 2000 rpm. After 5 mL of the supernatant was collected, it was replaced with an equal volume of fresh HBSS. The ionic concentration of the supernatant was subsequently analyzed using inductively coupled plasma-atomic emission spectrometry (ICP-AES, AGILENT 725-ES, USA).

4.4. Animal surgery

C57BL/6J male mice (wild type, WT) were purchased from the Animal Center of Nanjing Medical University. The *Atg5$^{flox/flox}$* (*Atg5$^{f/f}$*) mice and *Prx1-Cre* mice were obtained from the Model Animal Research Center of Nanjing University. *Atg5$^{f/f}$* mice and homozygous *Prx1-Cre* mice were crossed to obtain *Prx1-Cre; Atg5$^{f/f}$* mice. 12-week-old male mice were used for constructing of femoral defect model. After anesthetized with intraperitoneal administration of 1 % sodium pentobarbital (0.1 mL/10 g body weight) and skin incision, the medial surfaces of bilateral distal femurs were exposed by blunt dissection of the muscles. A hole defect of 1.2 mm diameter was prepared by round bur with saline irrigating. WT mice were randomly divided into 3 groups: (1) sham surgery group; (2) MBGNs group; (3) Cu-MBGNs group. *Prx1-Cre* mice and *Prx1-Cre; Atg5$^{f/f}$* mice were randomly divided into 2 groups respectively: MBGNs group and Cu-MBGNs group. Sodium citrate-coated microhematocrit tubes were used to collect the blood exuding from the defect to create the autologous blood clot. Then, for MBGNs groups and Cu-MBGNs groups, 20 μL of blood mixed with 0.75 mg MBGNs or Cu-MBGNs respectively dispersing in 0.8 μL PBS and 0.7 μL thrombin was induced to coagulating to obtain the blood clots. For the sham surgery group, pure PBS without MBGNs was used instead. After the autologous blood clots were placed in the defect, muscles and skin were sutured hierarchically and the mice were intramuscularly injected with penicillin G sodium salt to prevent infection.

4.5. Micro-CT analysis

In order to assess the formation of new bone in defect, the micro-CT scans were performed at 0, 14 and 28 days after the surgery. After anesthetized, the mice were scanned with a live animal scanning device (NewTom, Italy) on defect sites with high resolution of 18 μm and energy of 50 kV and 456 μA. NRecon, CTvox and CTan (SkyScan, Germany) software were used to reconstruct the 3D images of the bone and to analyze the bone volume ratio (BV/TV, %), trabecular thickness (Tb. Th.), trabecular number (Tb. N.) and bone mineral density (BMD) of the defect.

4.6. Fluorochrome labeling

With the aim to observe the bone mineralization within the defects, calcein (20 mg/kg) and alizarin red S (30 mg/kg) were subcutaneously injected into mice at the 8th and 2nd days before sacrifice respectively. The undecalcified femurs were fixed and dehydrated in 75–100 % gradient ethanol. After being soaked in and saturated with diluted resins under the vacuum condition, the samples were embedded in pure resin blocks. Then, slices with the thickness of 150 μm were cut by hard tissue microtome (EXAKT, Germany) and were thinned to the thickness of 50 μm with grinding (EXAKT, Germany). The pictures were captured by fluorescence microscopy (Leica, Germany) and the intensity of fluorescence was calculated by ImageJ software (NIH, USA).

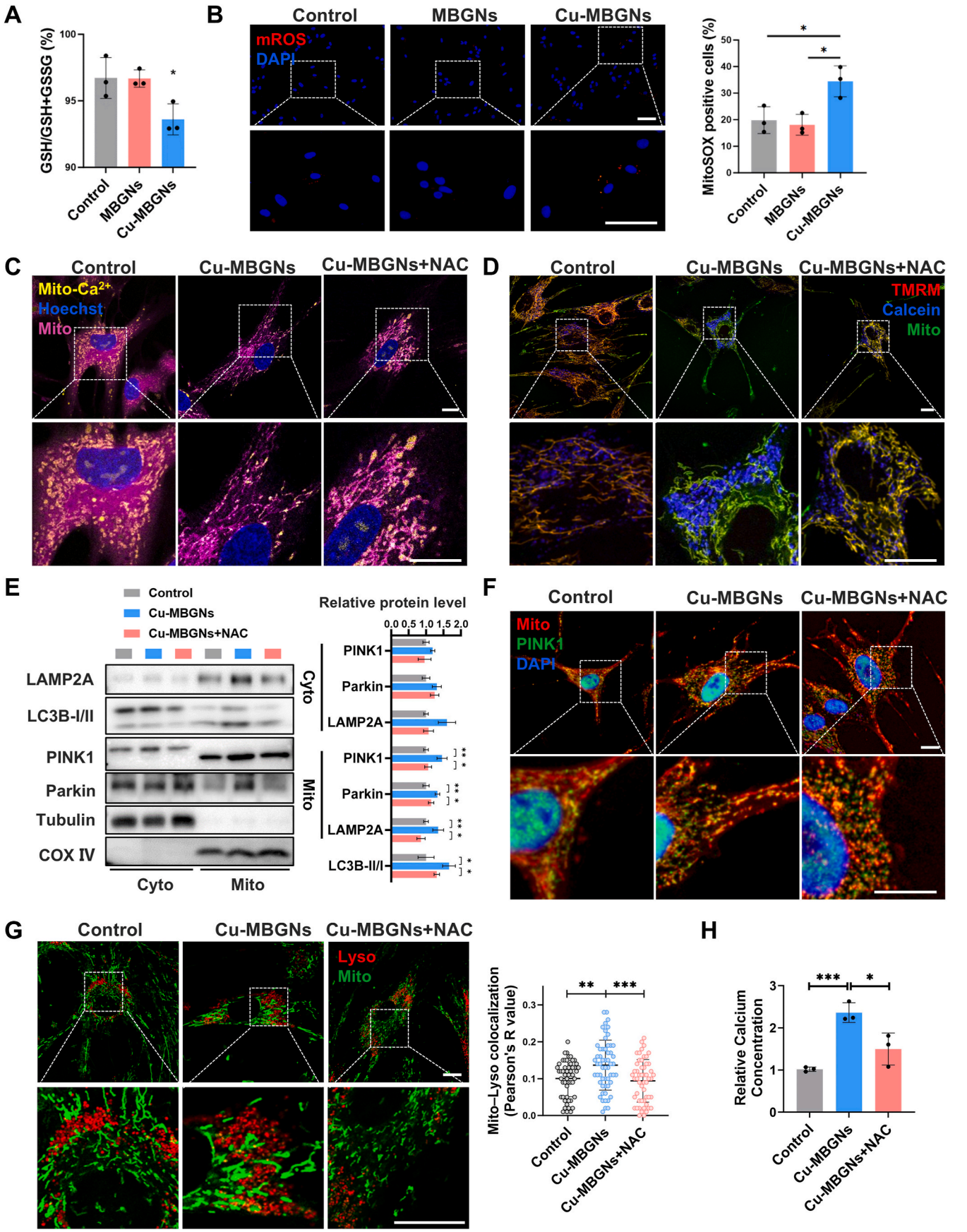

(caption on next page)

Fig. 6. Cu-MBGNs triggers mitophagy by binding with glutathione to increase mROS levels. **A)** Ratio of reduced GSH of osteoblast treated with conditioned medium from MBGNs or Cu-MBGNs for 6 h (n = 3). **B)** Representative images of MitoSOX of osteoblast treated with conditioned medium from MBGNs or Cu-MBGNs for 6 h (n = 3). Scale bars = 10 μm. **C)** Representative images of mitochondria and mitochondrial Ca^{2+} in osteoblasts treated with conditioned medium of Cu-MBGNs with or without NAC for 6 h (n = 3). Scale bars = 10 μm. **D)** Representative images of mitochondria, TMRM and Calcein in osteoblasts treated with conditioned medium of Cu-MBGNs with or without NAC for 6 h. Scale bars = 10 μm. **E)** WB images and relative level of mitophagy related proteins in cytoplasm and mitochondria of osteoblast treated with conditioned medium of Cu-MBGNs with or without NAC for 6 h (n = 3). **F)** Representative IF images of PINK1 and mitochondria in osteoblasts treated with conditioned medium of Cu-MBGNs with or without NAC for 6 h. Scale bars = 10 μm. **G)** Representative images and colocalization coefficient (Pearson's R value) of mitochondria and lysosomes in osteoblasts treated with conditioned medium of Cu-MBGNs with or without NAC for 6 h (n = 3). Scale bars = 10 μm. **H)** Calcium concentration of MV isolated from osteoblasts treated with conditioned medium of Cu-MBGNs with or without NAC for 1 week (n = 3). $^{*}p < 0.05$, $^{**}p < 0.01$, $^{***}p < 0.001$, ns $p > 0.05$.

4.7. Histological analysis

Hematoxylin-eosin (HE) staining and Masson staining were conducted to assess the bone regeneration in the defect area. Femur samples were fixed with 4 % paraformaldehyde solution and decalcified with 12.5 % ethylenediaminetetraacetic acid for 6 weeks. Then samples were dehydrated with 15 % and 30 % sucrose solution for 1d each and embedded in optimal cutting temperature compound for frozen section. After cut into 6 μm-thick slices, sections were stained with HE and Masson according to the manufacturer's steps (Beyotime, China).

4.8. Cell culture and differentiation

Human BMSCs were applied *in vitro* studies and isolated according to previous studies. Volunteers were fully informed and consented with the experiment. The inclusion criteria and cell culture protocols were conducted as previously described [75]. In brief, cancellous bones of jaws were divided into small pieces, wetted with minimum essential medium α (MEM α) (Thermo Fisher Scientific, USA) supplemented with 10 % FBS (ScienCell, USA), 100 U/mL penicillin and 100 μg/mL streptomycin, regarded as complete medium, and adhered on culture plate for 6 h. Then bone pieces were supplemented and cultured with complete medium for 5–7 d. When reached 80%–90 % confluence, BMSCs were passaged and the media were replaced every 3 d. The third to fifth passages of BMSCs were used for the following studies. Osteoblasts utilized in this study were induced from BMSCs with osteogenic medium which were composed of complete medium, 50 μM ascorbic acid, 10 mM β-glycerophosphate and 10^{-7} M dexamethasone for at least 7 d.

To obtain the conditioned medium, 1 mg/mL MBGNs or Cu-MBGNs were disperse and soaked in MEM α under continuous mixing conditions at 37 °C for 24 h, then the supernatant was collected and filtrated with 0.22 μm filter. During cell culture, MEM α was used to dilute the conditioned medium to different concentrations from 0 to 100 % (v/v).

4.9. Cytotoxicity and cell proliferation

The cytotoxicity and effect of MBGNs and Cu-MBGNs on the proliferation of BMSCs was evaluated by cell counting kit-8 (CCK8, apexbio). BMSCs were seeded in 96-well plate and cultured with conditioned medium for 1,3,5 and 7d respectively. At each point of time, the 10 % CCK-8 in fresh MEM α was replaced and the optical density (OD) value was measured at the wavelength of 450 nm with a microplate reader (SpectraMax 340, Molecular Devices, USA).

4.10. Inhibitors

50 nM Bafilomycin A1 (Abcam, UK) was used as a lysosomal proton adenosine triphosphatase inhibitor to detect changes in autophagic flux and was added 4 h before protein extraction. Cyclosporin A (CsA, MCE, China) was used as the inhibitor of mitophagy with the working concentration of 50 nM. N-acetylcysteine (NAC, Beyotime, China), as an antioxidant, was applied with the working concentration of 500 μM. Mdivi-1 (Beyotime, China) was used as the inhibitor of mitochondrial fission with the working concentration of 1 μM. Inhibitors were added to the conditioned medium to incubate cells.

4.11. SEM and TEM analysis on cells

Osteoblasts co-cultured with MBGNs or Cu-MBGNs and their conditioned medium for 6 h were fixed in 2.5 % glutaraldehyde for 2 h at room temperature and subsequently dehydrated using a series of ethanol solutions. Following gold sputtering treatment, the samples were imaged and characterized with SEM. To observe subcellular structure, cells were fixed with 2.5 % glutaraldehyde, followed by fixation with 1 % osmium tetroxide solution for 2 h. Cells were dehydrated in ethanol and embedded in alkoxy resin and made into ultra-thin sections. Following preparation, the sections were stained with uranyl acetate and lead citrate, and then examined using TEM.

4.12. Alizarin red S (ARS) staining

Alizarin red staining was used to evaluate the mineralization ability of osteoblasts *in vitro*. After undergoing 7 d of osteogenic induction from BMSCs, osteoblasts were cultured with conditioned osteogenic medium of MBGNs or Cu-MBGNs for 14 d. Subsequently, cells were fixed with 75 % ethanol and stained with ARS (Beyotime, China). The calcified nodules were identified and taken pictures with under inverted microscope (Leica, Germany). To quantify the deposition of calcium, the staining was dissolved in 10 % cetylpyridinium chloride and its absorbance value was measured at 450 nm.

4.13. Isolation of matrix vesicles (MVs)

After 7 d of osteoinduction and 14 d of culture with conditioned osteogenic medium of MBGNs or Cu-MBGNs, cells growth on 10 cm plate were incubated with collagenase for 30 min at 37 °C to digest ECM to liberate MVs. Then the samples were centrifuged at 2000g for 10 min to exclude cells and the supernatants were further centrifuged at 10000g for 30 min at 4 °C to remove cell debris. After the ultracentrifugation of the supernatants at 100,000g for 60 min, the precipitate was resuspended with to obtain MVs and the protein concentration of MVs was evaluated with the Bradford assay. Then the MVs were lysed in 0.1 M HCl and normalized with protein concentration, the calcium contents of lysis were determined by calcium colorimetric assay kit.

4.14. Live cell imaging

Live cell imaging was conducted with STED laser confocal microscopy (Leica, German) to observe the mitochondrial membrane potential (MMP), ACP, mROS and the distribution of mitochondria and lysosome. To label intracellular ACP, 1 mg/mL Calcein Blue (MCE, China) was added to the culture medium the day before the imaging. After cultured with conditioned osteogenic medium for 6 h, osteoblasts growing on glass bottom cell culture dishes were stained with tetramethylrhodamine methyl ester (TMRM, abcam, UK) and Mito-Tracker Green (Beyotime, China) at 37 °C for 30 min to detect MMP levels. To evaluate the level of mROS, cells were stained with MitoSOX (Beyotime, China) and Hoechst (Beyotime, China) at 37 °C for 30 min. To evaluate the level of mitophagy, cells were stained with Mito-Tracker Green (Beyotime, China) and Lyso-Tracker Red (Beyotime, China) fluorescence probes at 37 °C for 30 min. During the image acquisition process, cells

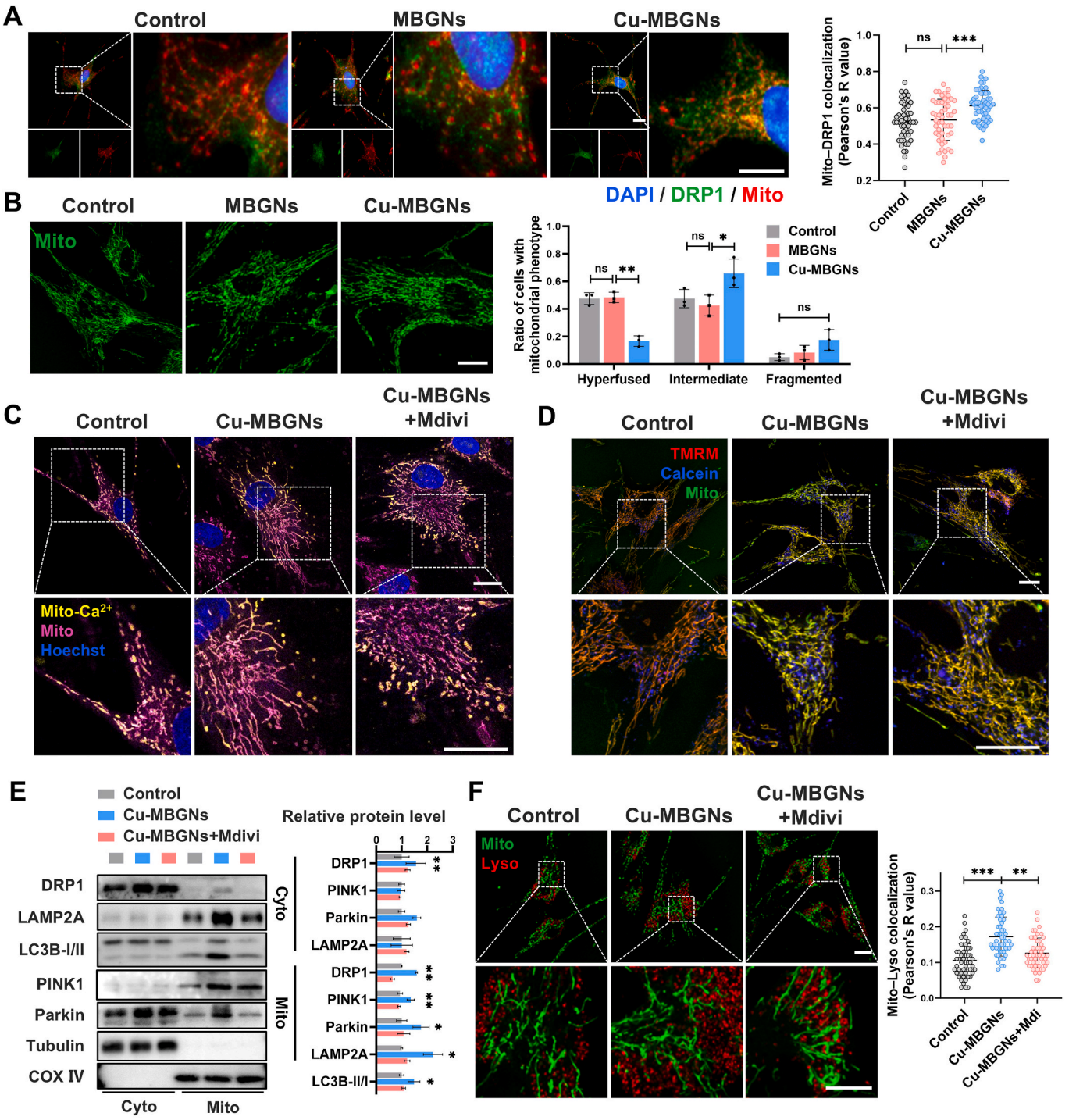

(caption on next page)

Fig. 7. Cu-MBGNs induce mitophagy by enhancing the process of mitochondrial fission. **A)** Representative IF images and colocalization coefficient of Drp1 and mitochondria in osteoblasts treated with conditioned medium of MBGNs or Cu-MBGNs for 6 h (n = 3). Scale bars = 10 μm. **B)** Representative images of mitochondrial morphology of osteoblast treated with conditioned medium from MBGNs or Cu-MBGNs for 6 h and proportion of cells with different mitochondrial morphologies (n = 3). Scale bar = 10 μm. **C)** Representative images of mitochondria and mitochondrial Ca^{2+} in osteoblasts treated with conditioned medium of Cu-MBGNs with or without Mdivi for 6 h. Scale bars = 10 μm. **D)** Representative images of mitochondria, TMRM and Calcein in osteoblasts treated with conditioned medium of Cu-MBGNs with or without Mdivi for 6 h. Scale bars = 10 μm. **E)** WB images and relative level of mitophagy related proteins in cytoplasm and mitochondria of osteoblast treated with conditioned medium of Cu-MBGNs with or without Mdivi for 6 h (n = 3). **F)** Representative images and colocalization coefficient of mitochondria and lysosomes in osteoblasts treated with conditioned medium of Cu-MBGNs with or without Mdivi for 6 h (n = 3). Scale bar = 10 μm and 5 μm (enlarged figures). **G)** Calcium concentration of MV isolated from osteoblasts treated with conditioned medium of Cu-MBGNs with or without Mdivi for 1 week (n = 3). **H)** ARS staining and quantitative analysis of mineralized nodules of osteoblasts treated with conditioned medium of Cu-MBGNs with or without Mdivi for 2 weeks (n = 3). $*p < 0.05$, $**p < 0.01$, $***p < 0.001$, ns $p > 0.05$.

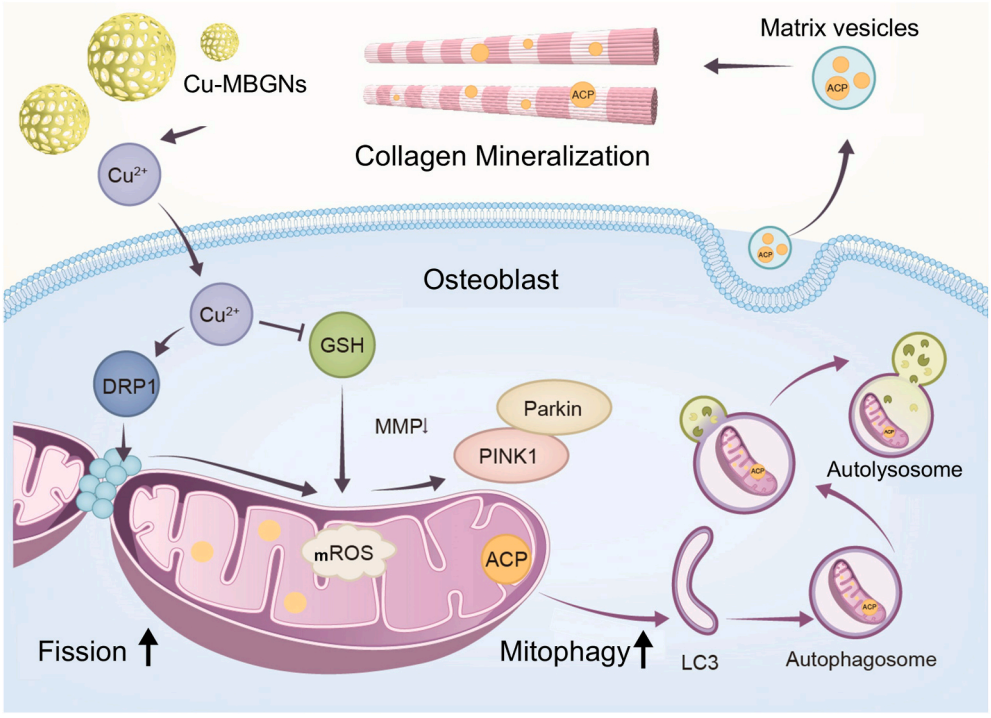

Fig. 8. This schematic illustrates the mechanism of Cu-MBGNs facilitating osteoblast mitophagy and mitochondrial dynamics, which enhance ACP release and subsequent biomineralization, ultimately accelerating the process of bone regeneration.

were incubated in live cell imaging solution (Gibco, USA).

4.15. Immunofluorescence (IF)

Osteoblasts seeded on cover glasses were cultured with conditioned osteogenic medium for 6 h and stained with Mito-Tracker Red CMXRos (Beyotime, China) before fixed in 4 % paraformaldehyde. For histological immunofluorescence, frozen sections were prepared as mentioned before. Samples were subsequently permeabilized with 0.1 % Tween-20 and blocked with goat serum, then samples were incubated with primary antibody at 4 °C overnight. After washed in PBS for 3 times, samples were incubated with Cy3-labeled or FITC-labeled secondary IgG at 37 °C for 1 h and then stained with DAPI for 3 min at room temperature. Fluorescence microscopy was used to capture the images.

4.16. Mitochondria isolation

Mitochondria isolation was conducted to observe the recruitment of protein on mitochondria according to the method of the mitochondria isolation kit (Beyotime, China). First, osteoblasts cultured with conditioned osteogenic medium for 6 h were collected with trypsin/EDTA solution (Gibco, USA) and resuspended with 1 mL of separation reagent, then cells were homogenized with a glass homogenizer until 50 % of cells can be dyed by trypan blue. Second, the cell homogenates were centrifugated at 600 g and 4 °C for 10 min and the supernatants were centrifugated at 11000 g for 10 min. The supernatants were collected as cytoplasmic (Cyto) protein without mitochondria and the precipitates were lysed to obtain mitochondrial (Mito) protein.

4.17. Protein extraction

For total protein extraction, cells were lysed with RIPA lysis buffer (Beyotime, China) containing protease inhibitors, centrifuged at 12000 g for 5 min, and the supernatant was taken. After adding SDS-PAGE sample loading buffer, the total, Cyto or Mito protein samples were subjected to a metal bath at 100 °C for 5 min.

4.18. Western blot (WB)

Sodium dodecyl sulfate-polyacrylamide gel electrophoresis was used to conduct Western blot. Protein samples were loaded onto polyacrylamide gel and were transferred to PVDF membranes (Millipore, USA) after gel electrophoresis. Subsequently, membranes were blocked with skim milk and incubated with primary antibodies at 4 °C overnight. Then membranes were washed with TBST and incubated with HRP-conjugated secondary antibodies. Lastly, protein bands were detected with ECL western blotting substrate (Tanon, China) and visualized with chemiluminescence image analysis system (Tanon, China). Actin,

Tubulin and COX IV signal intensities were used for normalization of total, cytoplasmic and mitochondrial protein respectively.

Antibodies of Collagen I, OCN, TOM20, PINK1, Parkin, p62, DRP1, COX IV, β-Tubulin, β-Actin and secondary antibodies were purchased from Proteintech. Antibodies of CD31 and LAMP2A were purchased from Abcam. Antibody of LC3B were purchased from Cell Signaling Technology. Antibody of EMCN were purchased from Santa Cruz Biotechnology.

4.19. ATP concentration testing

To test the synthesis of ATP, cells were lysed with lysis buffer and centrifuged at 4 °C for 5 min at 12,000 g to collect the supernatant. Standard curve was prepared following the ATP Testing Kit (Beyotime, China)'s instructions. ATP detection working solution and sample or standard were mixed and measured for luminescence using a luminometer.

4.20. Flow cytometry analysis

For detection of intracellular calcium ion, cells were harvested and grinded for single-cell suspension. Then cells were washed with PBS and stained with Fluo-3 AM probes (Beyotime, China) at 37 °C for 30 min. Flow cytometry was performed with a BD FACSymphony A5 flow cytometer. All flow cytometry data were then analyzed with FlowJo v.10 software.

4.21. Reduced GSH content test

To test the ratio of GSH/GSSG, osteoblasts treated with conditioned osteogenic medium for 6 h was lysed by freezing and thawing in liquid nitrogen and water bath. Then following the GSH and GSSG Assay Kit (Beyotime, China)'s instructions, total GSH content, reduced GSH and GSSG content were determined by microplate reader and calculated.

4.22. Statistical analysis

The results are presented as means ± standard deviation (SD). Each *in vitro* experiment was independently repeated at least three times to ensure reliability. Statistical significance for comparisons between two groups was assessed using Student's t-test, while analysis across multiple groups was conducted using one-way analysis of variance (ANOVA). $*p < 0.05$; $**p < 0.01$; $***p < 0.001$ were considered statistically significant.

CRediT authorship contribution statement

Ziji Ling: Writing – original draft, Visualization, Methodology, Investigation, Formal analysis, Data curation. **Xiao Ge:** Software, Formal analysis, Data curation. **Chengyu Jin:** Investigation, Data curation. **Zesheng Song:** Investigation. **Hang Zhang:** Investigation. **Yu Fu:** Supervision, Resources, Project administration. **Kai Zheng:** Resources, Project administration, Conceptualization. **Rongyao Xu:** Writing – review & editing, Supervision, Resources, Project administration, Conceptualization. **Hongbing Jiang:** Writing – review & editing, Writing – original draft, Validation, Supervision, Resources, Project administration, Methodology, Funding acquisition, Conceptualization.

Data availability

The data of this research are available from the corresponding author upon reasonable request.

Ethics approval and consent to participate

According to the guidelines of the Animal Care Committee of the School of Stomatology, Nanjing Medical University, all experiments were approved by the Ethics Committee (Approval No. IACUC-2410068). All procedures involving human BMSCs were approved by the Ethical Committee of the Affiliated Hospital of Stomatology, Nanjing Medical University (Approval No. PJ2018-047-001). Volunteers were fully informed and consented with the experiment.

Declaration of competing interest

The authors declare that they have no competing interests.

Acknowledgements

This work was supported by the National Natural Science Foundation of China (81771092, 81970910 and 82370931), Jiangsu Province Capability Improvement Project through Science, Technology and Education-Jiangsu Provincial Research Hospital Cultivation Unit (YJXYYJSDW4) and Jiangsu Provincial Medical Innovation Center (CXZX202227).

We would like to thank Yongchu Pan, Mifang Yang, Donglin Yan, Linlin Jiang, Kang Li, and Lan Ma for their guidance in the utilization of experimental instruments (State Key Laboratory Cultivation Base of Research, Prevention and Treatment for Oral Diseases, Nanjing Medical University). We would like to thank Huiwen Zhang for laser confocal microscope imaging (Jiangsu Province Hospital Core Facility Center, Nanjing Medical University).

Appendix A. Supplementary data

Supplementary data to this article can be found online at https://doi.org/10.1016/j.bioactmat.2024.12.010.

Abbreviations

Cu-MBGNs	copper doped mesoporous bioactive glass nanoparticles
ACP	amorphous calcium phosphate
Drp1	dynamin related protein 1
ECM	extracellular matrix
MMP	mitochondrial membrane potential
ROS	reactive oxygen species
mROS	mitochondrial reactive oxygen species
SEM	scanning electron microscope
TEM	Transmission electron microscope
EDS	Energy Dispersive spectroscopy
XPS	X-ray photoelectron spectroscopy
BMD	bone mineral density
BV/TV	bone volume fraction
Tb. Th	trabecular thickness
Tb. N	trabecular number
EMCN	Endomucin
OCN	osteocalcin
COL-I	collagen Type I
ARS	alizarin red S
N.Ob/B.pm	number of osteoblast number per bone perimeter
Tb. MAR	trabecular mineralization apposition rate
CKO	conditional knockout
PRX1	paired related homeobox 1
BMSCs	bone marrow mesenchymal stem cells
MVs	Matrix vesicles
Baf A1	bafilomycin A1
TMRM	tetramethylrhodamine methyl ester
MFI	mean fluorescence intensity
CsA	Cyclosporin A
GSH	glutathione
Cyto	cytoplasmic
Mito	mitochondrial

Lyso lysosome

References

[1] T. Gong, J. Xie, J. Liao, T. Zhang, S. Lin, Y. Lin, Nanomaterials and bone regeneration, Bone Research 3 (2015) 15029.
[2] H. Wei, J. Cui, K. Lin, J. Xie, X. Wang, Recent advances in smart stimuli-responsive biomaterials for bone therapeutics and regeneration, Bone Res. 10 (2022) 17.
[3] P. Feng, P. Wu, C. Gao, Y. Yang, W. Guo, W. Yang, C. Shuai, A multimaterial scaffold with tunable properties: toward bone tissue repair, Adv. Sci. 5 (2018) 1700817.
[4] A. Salhotra, H.N. Shah, B. Levi, M.T. Longaker, Mechanisms of bone development and repair, Nat. Rev. Mol. Cell Biol. 21 (2020) 696–711.
[5] G.N. Duda, S. Geissler, S. Checa, S. Tsitsilonis, A. Petersen, K. Schmidt-Bleek, The decisive early phase of bone regeneration, Nat. Rev. Rheumatol. 19 (2023) 78–95.
[6] C. Shuai, W. Yang, P. Feng, S. Peng, H. Pan, Accelerated degradation of HAP/PLLA bone scaffold by PGA blending facilitates bioactivity and osteoconductivity, Bioact. Mater. 6 (2021) 490–502.
[7] C.S. Kovacs, C. Chaussain, P. Osdoby, M.L. Brandi, B. Clarke, R.V. Thakker, The role of biomineralization in disorders of skeletal development and tooth formation, Nat. Rev. Endocrinol. 17 (2021) 336–349.
[8] X. Yan, Q. Zhang, X. Ma, Y. Zhong, H. Tang, S. Mai, The mechanism of biomineralization: progress in mineralization from intracellular generation to extracellular deposition, Jpn Dent Sci Rev. 59 (2023) 181–190.
[9] C. Tang, Y. Wei, L. Gu, Q. Zhang, M. Li, G. Yuan, Y. He, L. Huang, Y. Liu, Y. Zhang, Biomineral precursor formation is initiated by transporting calcium and phosphorus clusters from the endoplasmic reticulum to mitochondria, Adv. Sci. 7 (2020) 1902536.
[10] D.D. Pei, J.L. Sun, C.H. Zhu, F.C. Tian, K. Jiao, M.R. Anderson, C. Yiu, C. Huang, C. X. Jin, B.E. Bergeron, J.H. Chen, F.R. Tay, L.N. Niu, Contribution of mitophagy to cell-mediated mineralization: revisiting a 50-year-old conundrum, Adv. Sci. 5 (2018) 1800873.
[11] T. Iwayama, T. Okada, T. Ueda, K. Tomita, S. Matsumoto, M. Takedachi, S. Wakisaka, T. Noda, T. Ogura, T. Okano, P. Fratzl, T. Ogura, S. Murakami, Osteoblastic lysosome plays a central role in mineralization, Sci. Adv. 5 (2019) eaax0672.
[12] T. Hasegawa, H. Hongo, T. Yamamoto, M. Abe, H. Yoshino, M. Haraguchi-Kitakamae, H. Ishizu, T. Shimizu, N. Iwasaki, N. Amizuka, Matrix vesicle-mediated mineralization and osteocytic regulation of bone mineralization, Int. J. Mol. Sci. 23 (2022).
[13] J. Wang, Y. Zhang, J. Cao, Y. Wang, N. Anwar, Z. Zhang, D. Zhang, Y. Ma, Y. Xiao, L. Xiao, X. Wang, The role of autophagy in bone metabolism and clinical significance, Autophagy 19 (2023) 2409–2427.
[14] W. Ling, K. Krager, K.K. Richardson, A.D. Warren, F. Ponte, N. Aykin-Burns, S. C. Manolagas, M. Almeida, H.N. Kim, Mitochondrial Sirt3 contributes to the bone loss caused by aging or estrogen deficiency, JCI Insight 6 (2021).
[15] D. Li, D. Dai, J. Wang, C. Zhang, Honeycomb bionic graphene oxide quantum dot/layered double hydroxide composite nanocoating promotes osteoporotic bone regeneration via activating mitophagy, Small (2024) e2403907.
[16] Y. Liu, S. Lin, Z. Xu, Y. Wu, G. Wang, G. Yang, L. Cao, H. Chang, M. Zhou, X. Jiang, High-performance hydrogel-encapsulated engineered exosomes for supporting endoplasmic reticulum homeostasis and boosting diabetic bone regeneration, Adv. Sci. 11 (2024) e2309491.
[17] J. Cui, X. Zhang, L. Cheng, K. Lin, Autophagy mediates osteoporotic bone regeneration induced by micro-/nano-structured modification on hydroxyapatite bioceramics, Engineered Regeneration 4 (2023) 245–256.
[18] S. Yao, Y. Xu, Y. Zhou, C. Shao, Z. Liu, B. Jin, R. Zhao, H. Cao, H. Pan, R. Tang, Calcium phosphate nanocluster-loaded injectable hydrogel for bone regeneration, ACS Appl. Bio Mater. 2 (2019) 4408–4417.
[19] S. Yao, X. Lin, Y. Xu, Y. Chen, P. Qiu, C. Shao, B. Jin, Z. Mu, N. Sommerdijk, R. Tang, Osteoporotic bone recovery by a highly bone-inductive calcium phosphate polymer-induced liquid-precursor, Adv. Sci. 6 (2019) 1900683.
[20] S. Tang, Z. Dong, X. Ke, J. Luo, J. Li, Advances in biomineralization-inspired materials for hard tissue repair, Int. J. Oral Sci. 13 (2021) 42.
[21] E.J. Ge, A.I. Bush, A. Casini, P.A. Cobine, J.R. Cross, G.M. DeNicola, Q.P. Dou, K. J. Franz, V.M. Gohil, S. Gupta, S.G. Kaler, S. Lutsenko, V. Mittal, M.J. Petris, R. Polishchuk, M. Ralle, M.L. Schilsky, N.K. Tonks, L.T. Vahdat, L. Van Aelst, D. Xi, P. Yuan, D.C. Brady, C.J. Chang, Connecting copper and cancer: from transition metal signalling to metalloplasia, Nat. Rev. Cancer 22 (2022) 102–113.
[22] V.N. Pham, C.J. Chang, Metalloallostery and transition metal signaling: bioinorganic copper chemistry beyond active sites, Angew Chem Int Ed Engl. 62 (2023) e202213644.
[23] H. Zhu, M. Monavari, K. Zheng, T. Distler, L. Ouyang, S. Heid, Z. Jin, J. He, D. Li, A. R. Boccaccini, 3D bioprinting of multifunctional dynamic nanocomposite bioinks incorporating Cu-doped mesoporous bioactive glass nanoparticles for bone tissue engineering, Small 18 (2022) e2104996.
[24] I. Burghardt, F. Lüthen, C. Prinz, B. Kreikemeyer, C. Zietz, H.G. Neumann, J. Rychly, A dual function of copper in designing regenerative implants, Biomaterials 44 (2015) 36–44.
[25] Y. Xu, C. Xu, K. Yang, L. Ma, G. Li, Y. Shi, X. Feng, L. Tan, D. Duan, Z. Luo, C. Yang, Copper ion-modified germanium phosphorus nanosheets integrated with an electroactive and biodegradable hydrogel for neuro-vascularized bone regeneration, Adv. Healthcare Mater. (2023) e2301151.
[26] G. Jian, D. Li, Q. Ying, X. Chen, Q. Zhai, S. Wang, L. Mei, R.D. Cannon, P. Ji, W. Liu, H. Wang, T. Chen, Dual photo-enhanced interpenetrating network hydrogel with biophysical and biochemical signals for infected bone defect healing, Adv. Healthcare Mater. (2023) e2300469.
[27] N.M. Garza, A.B. Swaminathan, K.P. Maremanda, M. Zulkifli, V.M. Gohil, Mitochondrial copper in human genetic disorders, Trends Endocrinol. Metabol. 34 (2023) 21–33.
[28] L.M. Ruiz, A. Libedinsky, A.A. Elorza, Role of copper on mitochondrial function and metabolism, Front. Mol. Biosci. 8 (2021).
[29] P. Tsvetkov, S. Coy, B. Petrova, M. Dreishpoon, A. Verma, M. Abdusamad, J. Rossen, L. Joesch-Cohen, R. Humeidi, R.D. Spangler, J.K. Eaton, E. Frenkel, M. Kocak, S.M. Corsello, S. Lutsenko, N. Kanarek, S. Santagata, T.R. Golub, Copper induces cell death by targeting lipoylated TCA cycle proteins, Science. 375 (2022) 1254–1261.
[30] D. Murata, S. Roy, S. Lutsenko, M. Iijima, H. Sesaki, Slc25a3-dependent copper transport controls flickering-induced Opa1 processing for mitochondrial safeguard, Dev. Cell 59 (2024) 2578–2592.e7.
[31] R. Quintana-Cabrera, L. Scorrano, Determinants and outcomes of mitochondrial dynamics, Mol. Cell 83 (2023) 857–876.
[32] M.Y.W. Ng, T. Wai, A. Simonsen, Quality control of the mitochondrion, Dev. Cell 56 (2021) 881–905.
[33] M. Frank, S. Duvezin-Caubet, S. Koob, A. Occhipinti, R. Jagasia, A. Petcherski, M. O. Ruonala, M. Priault, B. Salin, A.S. Reichert, Mitophagy is triggered by mild oxidative stress in a mitochondrial fission dependent manner, Biochim. Biophys. Acta 1823 (2012) 2297–2310.
[34] H. Sies, D.P. Jones, Reactive oxygen species (ROS) as pleiotropic physiological signalling agents, Nat. Rev. Mol. Cell Biol. 21 (2020) 363–383.
[35] E.L. Jensen, A.M. Gonzalez-Ibanez, P. Mendoza, L.M. Ruiz, C.A. Riedel, F. Simon, J. J. Schuringa, A.A. Elorza, Copper deficiency-induced anemia is caused by a mitochondrial metabolic reprograming in erythropoietic cells, Metallomics 11 (2019) 282–290.
[36] K. Zhang, X. Meng, Z. Yang, H. Dong, X. Zhang, Enhanced cancer therapy by hypoxia-responsive copper metal-organic frameworks nanosystem, Biomaterials 258 (2020) 120278.
[37] G. Zhong, Y. Li, L. Li, Y. Huo, W. Zhang, T. Li, F. Ma, J. Liao, Y. Li, H. Zhang, J. Guo, J. Pan, W. Yu, L. Hu, Z. Tang, Mitochondrial miR-12294-5p regulated copper-induced mitochondrial oxidative stress and mitochondrial quality control imbalance by targeted inhibition of CISD1 in chicken livers, J. Hazard Mater. 458 (2023) 131908.
[38] L.M. Ruiz, E.L. Jensen, Y. Rossel, G.I. Puas, A.M. Gonzalez-Ibanez, R.I. Bustos, D. A. Ferrick, A.A. Elorza, Non-cytotoxic copper overload boosts mitochondrial energy metabolism to modulate cell proliferation and differentiation in the human erythroleukemic cell line K562, Mitochondrion 29 (2016) 18–30.
[39] M. Li, J. Shao, Z. Guo, C. Jin, L. Wang, F. Wang, Y. Jia, Z. Zhu, Z. Zhang, F. Zhang, S. Zheng, X. Wang, Novel mitochondrion-targeting copper(II) complex induces HK2 malfunction and inhibits glycolysis via Drp1-mediating mitophagy in HCC, J. Cell Mol. Med. 24 (2020) 3091–3107.
[40] F. Yang, J. Liao, W. Yu, N. Qiao, J. Guo, Q. Han, Y. Li, L. Hu, J. Pan, Z. Tang, Exposure to copper induces mitochondria-mediated apoptosis by inhibiting mitophagy and the PINK1/parkin pathway in chicken (Gallus gallus) livers, J. Hazard Mater. 408 (2021) 124888.
[41] Y. Fan, Z. Cheng, L. Mao, G. Xu, N. Li, M. Zhang, P. Weng, L. Zheng, X. Dong, S. Hu, B. Wang, X. Qin, X. Jiang, C. Chen, J. Zhang, Z. Zou, PINK1/TAX1BP1-directed mitophagy attenuates vascular endothelial injury induced by copper oxide nanoparticles, J. Nanobiotechnol. 20 (2022) 149.
[42] H. Autefage, F. Allen, H.M. Tang, C. Kallepitis, E. Gentleman, N. Reznikov, K. Nitiputri, A. Nommeots-Nomm, M.D. O'Donnell, C. Lange, B.M. Seidt, T.B. Kim, A.K. Solanki, F. Tallia, G. Young, P.D. Lee, B.F. Pierce, W. Wagermaier, P. Fratzl, A. Goodship, J.R. Jones, G. Blunn, M.M. Stevens, Multiscale analyses reveal native-like lamellar bone repair and near perfect bone-contact with porous strontium-loaded bioactive glass, Biomaterials 209 (2019) 152–162.
[43] K. Zheng, B. Sui, K. Ilyas, A.R. Boccaccini, Porous bioactive glass micro- and nanospheres with controlled morphology: developments, properties and emerging biomedical applications, Mater. Horiz. 8 (2021) 300–335.
[44] M.S. Kang, N.H. Lee, R.K. Singh, N. Mandakhbayar, R.A. Perez, J.H. Lee, H.W. Kim, Nanocements produced from mesoporous bioactive glass nanoparticles, Biomaterials 162 (2018) 183–199.
[45] C. Wu, J. Chang, Multifunctional mesoporous bioactive glasses for effective delivery of therapeutic ions and drug/growth factors, J. Contr. Release 193 (2014) 282–295.
[46] K. Zheng, J. Kang, B. Rutkowski, M. Gawęda, J. Zhang, Y. Wang, N. Founier, M. Sitarz, N. Taccardi, A.R. Boccaccini, Toward highly dispersed mesoporous bioactive glass nanoparticles with high Cu concentration using Cu/ascorbic acid complex as precursor, Front. Chem. 7 (2019) 497.
[47] Z. Wang, Q. Dai, H. Luo, X. Han, Q. Feng, X. Cao, Nano-vibration exciter: hypoxia-inducible factor 1 signaling pathway-mediated extracellular vesicles as bioactive glass substitutes for bone regeneration, Bioact. Mater. 40 (2024) 460–473.
[48] Z. Zhang, W. Li, D. Chang, Z. Wei, E. Wang, J. Yu, Y. Xu, Y. Que, Y. Chen, C. Fan, B. Ma, Y. Zhou, Z. Huan, C. Yang, F. Guo, J. Chang, A combination therapy for androgenic alopecia based on quercetin and zinc/copper dual-doped mesoporous silica nanocomposite microneedle patch, Bioact. Mater. 24 (2023) 81–95.
[49] A. Wajda, M. Sitarz, Structural and microstructural comparison of bioactive melt-derived and gel-derived glasses from CaO-SiO2 binary system, Ceram. Int. 44 (2018) 8856–8863.
[50] K. Zheng, A. Solodovnyk, W. Li, O.-M. Goudouri, C. Stähli, S.N. Nazhat, A. R. Boccaccini, Aging time and temperature effects on the structure and bioactivity of gel-derived 45S5 glass-ceramics, J. Am. Ceram. Soc. 98 (2015) 30–38.

[51] Q. Dai, Q. Li, H. Gao, L. Yao, Z. Lin, D. Li, S. Zhu, C. Liu, Z. Yang, G. Wang, D. Chen, X. Chen, X. Cao, 3D printing of Cu-doped bioactive glass composite scaffolds promotes bone regeneration through activating the HIF-1α and TNF-α pathway of hUVECs, Biomater. Sci. 9 (2021) 5519–5532.
[52] C. Wu, Y. Zhou, M. Xu, P. Han, L. Chen, J. Chang, Y. Xiao, Copper-containing mesoporous bioactive glass scaffolds with multifunctional properties of angiogenesis capacity, osteostimulation and antibacterial activity, Biomaterials 34 (2013) 422–433.
[53] Y. Zhou, S. Han, L. Xiao, P. Han, S. Wang, J. He, J. Chang, C. Wu, Y. Xiao, Accelerated host angiogenesis and immune responses by ion release from mesoporous bioactive glass, J. Mater. Chem. B 6 (2018) 3274–3284.
[54] J.P. Rodríguez, S. Ríos, M. González, Modulation of the proliferation and differentiation of human mesenchymal stem cells by copper, J. Cell. Biochem. 85 (2002) 92–100.
[55] H. Guo, Y. Ouyang, H. Yin, H. Cui, H. Deng, H. Liu, Z. Jian, J. Fang, Z. Zuo, X. Wang, L. Zhao, Y. Zhu, Y. Geng, P. Ouyang, Induction of autophagy via the ROS-dependent AMPK-mTOR pathway protects copper-induced spermatogenesis disorder, Redox Biol. 49 (2022) 102227.
[56] F. Wan, G. Zhong, Z. Ning, J. Liao, W. Yu, C. Wang, Q. Han, Y. Li, J. Pan, Z. Tang, R. Huang, L. Hu, Long-term exposure to copper induces autophagy and apoptosis through oxidative stress in rat kidneys, Ecotoxicol. Environ. Saf. 190 (2020) 110158.
[57] J.N.S. Vargas, M. Hamasaki, T. Kawabata, R.J. Youle, T. Yoshimori, The mechanisms and roles of selective autophagy in mammals, Nat. Rev. Mol. Cell Biol. 24 (2023) 167–185.
[58] B. Levine, G. Kroemer, Biological functions of autophagy genes: a disease perspective, Cell 176 (2019) 11–42.
[59] Z. Tian, S. Jiang, J. Zhou, W. Zhang, Copper homeostasis and cuproptosis in mitochondria, Life Sci. 334 (2023) 122223.
[60] S. Solier, S. Müller, T. Cañeque, A. Versini, A. Mansart, F. Sindikubwabo, L. Baron, L. Emam, P. Gestraud, G.D. Pantoș, V. Gandon, C. Gaillet, T.D. Wu, F. Dingli, D. Loew, S. Baulande, S. Durand, V. Sencio, C. Robil, F. Trottein, D. Péricat, E. Näser, C. Cougoule, E. Meunier, A.L. Bègue, H. Salmon, N. Manel, A. Puisieux, S. Watson, M.A. Dawson, N. Servant, G. Kroemer, D. Annane, R. Rodriguez, A druggable copper-signalling pathway that drives inflammation, Nature 617 (2023) 386–394.
[61] E.V. Polishchuk, A. Merolla, J. Lichtmannegger, A. Romano, A. Indrieri, E. Y. Ilyechova, M. Concilli, R. De Cegli, R. Crispino, M. Mariniello, R. Petruzzelli, G. Ranucci, R. Iorio, F. Pietrocola, C. Einer, S. Borchard, A. Zibert, H.H. Schmidt, E. Di Schiavi, L.V. Puchkova, B. Franco, G. Kroemer, H. Zischka, R.S. Polishchuk, Activation of autophagy, observed in liver tissues from patients with wilson disease and from ATP7B-deficient animals, protects hepatocytes from copper-induced apoptosis, Gastroenterology 156 (2019) 1173–1189.e5.
[62] L.N. Niu, S.E. Jee, K. Jiao, L. Tonggu, M. Li, L. Wang, Y.D. Yang, J.H. Bian, L. Breschi, S.S. Jang, J.H. Chen, D.H. Pashley, F.R. Tay, Collagen intrafibrillar mineralization as a result of the balance between osmotic equilibrium and electroneutrality, Nat. Mater. 16 (2017) 370–378.
[63] Y. Zhuang, S. Jiang, X. Deng, A. Lao, X. Hua, Y. Xie, L. Jiang, X. Wang, K. Lin, Energy metabolism as therapeutic target for aged wound repair by engineered extracellular vesicle, Sci. Adv. 10 (2024) eadl0372.
[64] M.Y.W. Ng, T. Wai, A. Simonsen, Quality control of the mitochondrion, Dev. Cell 56 (2021) 881–905.
[65] I. Dikic, Z. Elazar, Mechanism and medical implications of mammalian autophagy, Nat. Rev. Mol. Cell Biol. 19 (2018) 349–364.
[66] W. Springer, P.J. Kahle, Regulation of PINK1-Parkin-mediated mitophagy, Autophagy 7 (2011) 266–278.
[67] J.H. Freedman, M.R. Ciriolo, J. Peisach, The role of glutathione in copper metabolism and toxicity, J. Biol. Chem. 264 (1989) 5598–5605.
[68] N. Ishihara, Y. Eura, K. Mihara, Mitofusin 1 and 2 play distinct roles in mitochondrial fusion reactions via GTPase activity, J. Cell Sci. 117 (2004) 6535–6546.
[69] M. Rojo, F. Legros, D. Chateau, A. Lombès, Membrane topology and mitochondrial targeting of mitofusins, ubiquitous mammalian homologs of the transmembrane GTPase Fzo, J. Cell Sci. 115 (2002) 1663–1674.
[70] T. Kleele, T. Rey, J. Winter, S. Zaganelli, D. Mahecic, H. Perreten Lambert, F. P. Ruberto, M. Nemir, T. Wai, T. Pedrazzini, S. Manley, Distinct fission signatures predict mitochondrial degradation or biogenesis, Nature 593 (2021) 435–439.
[71] L.M. Ruiz, E.L. Jensen, R.I. Bustos, G. Argüelloa, R. Gutierrez-Garcia, M. González, C. Hernández, R. Paredes, F. Simon, C. Riedel, D. Ferrick, A.A. Elorza, Adaptive responses of mitochondria to mild copper deprivation involve changes in morphology, OXPHOS remodeling and bioenergetics, J. Cell. Physiol. 229 (2014) 607–619.
[72] Y. Liu, H. Zhao, Y. Wang, M. Guo, M. Mu, M. Xing, Arsenic (III) and/or copper (II) induces oxidative stress in chicken brain and subsequent effects on mitochondrial homeostasis and autophagy, J. Inorg. Biochem. 211 (2020) 111201.
[73] Y. Zhu, X. Zhang, G. Chang, S. Deng, H.F. Chan, Bioactive glass in tissue regeneration: unveiling recent advances in regenerative strategies and applications, Adv. Mater. (2024) e2312964.
[74] D.S. Brauer, Bioactive glasses—structure and properties, Angew Chem Int Ed Engl. 54 (2015) 4160–4181.
[75] H. Zhang, R. Xu, B. Li, Z. Xin, Z. Ling, W. Zhu, X. Li, P. Zhang, Y. Fu, J. Chen, L. Liu, J. Cheng, H. Jiang, LncRNA NEAT1 controls the lineage fates of BMSCs during skeletal aging by impairing mitochondrial function and pluripotency maintenance, Cell Death Differ. 29 (2022) 351–365.